Size-velocity correlations in high order moment methods for polydisperse evaporating sprays: modelling and numerical issues

Aymeric Vié, Frédérique Laurent, Marc Massot

▶ To cite this version:

Aymeric Vié, Frédérique Laurent, Marc Massot. Size-velocity correlations in high order moment methods for polydisperse evaporating sprays: modelling and numerical issues. 2011. hal-00626869v2

HAL Id: hal-00626869

https://hal.science/hal-00626869v2

Preprint submitted on 12 Oct 2011 (v2), last revised 6 Aug 2012 (v3)

Size-velocity correlations in high order moment methods for polydisperse evaporating sprays: modelling and numerical issues

Aymeric Vié[a,b], Frédérique Laurent[a,b], Marc Massot[a,b,c]

[a] *CNRS, UPR 288, Laboratoire d'Energétique moléculaire et macroscopique, combustion, Grande Voie des Vignes, 92295 Chatenay-Malabry, France*
[b] *Ecole Centrale Paris, Grande Voie des Vignes, 92295 Chatenay-Malabry, France*
[c] *Center for Turbulence Research, Stanford University, California 94305-4035, USA*

Abstract

Kah et al. (2010) recently developed the Eulerian Multi-Size Moment model (EMSM) which tackles the modelling and the numerical aspects for the simulation of polydisperse multiphase flows of a gaseous flow field carrying a disperse liquid phase. Using a moment method, they proposed to reconstruct the number density function (NDF) by Entropy Maximization, which leads to a unique and realizable NDF. This reconstruction is used to simulate the evaporation process, by an evaluation of the flux of droplet disappearance at zero size and an accurate description of the size shift induced by evaporation. Although this method demonstrated its great potential for evaporating polydisperse flows, two issues remain to be addressed. First, the EMSM only considers one velocity for all droplets, thus decoupling size from velocity, which will be too restrictive for distributions with a large size spectrum. In most applications size-conditioned dynamics have to be accounted for. Second, the possibility to have separated dynamics for each size can lead to quasi-monodisperse distributions, which corresponds to a hard limiting case for the entropy maximization algorithm. So the behaviour of the entropy maximization needs to be investigated, in order to be able to reproduce a larger subset of the moment space. The aim of this paper is thus twofold. First, the entropy maximization and its related algorithm are enhanced by using a more precise integration method in order to handle NDF close to the frontier of the moment space associated with an adaptive number of parameters to reconstruct the NDF accurately and efficiently, as well as tabulated initial guess to optimize the computational time. Then, a new model called CSVM (Coupled Size-Velocity Moments model) is proposed. Size-velocity correlations are addressed either in the evaporation and drag processes, or in the convective transport. To reach this goal, a reconstruction of the velocity for each size is proposed, using only one additional moment per dimension. This reconstruction is evaluated in evaporation-drag 0D cases, to assess its ability to reproduce both phenomena. To handle the convective transport, a new flux splitting scheme is proposed, based on the underlying kinetic description of the disperse phase. The full strategy is evaluated in 1D and 2D cases and shows the ability of the CSVM and its related algorithms to capture the full physics of polydisperse evaporating sprays with a minimal number of moments.

Key words: Polydisperse sprays, high order moment method, Entropy Maximization, flux splitting, size-velocity correlations

---

1. Introduction

Multiphase flows occur in several industrial applications, such as internal combustion engine ([1, 2] and references therein), gas turbine [3] or rocket booster [4]. Those applications are linked by the existence of a

---

Email addresses: `aymeric.vie@em2c.ecp.fr` (Aymeric Vié), `frederique.laurent@em2c.ecp.fr` (Frédérique Laurent), `marc.massot@em2c.ecp.fr` (Marc Massot)

disperse liquid phase, composed of droplets. Simulating this disperse phase accurately becomes crucial, as it highly influences the global behaviour of the full device (consumption, overall power, pollutant emissions...).

The description of a disperse phase may rely on a population balance equation (PBE) on the number density function (NDF), namely the Williams-Boltzmann equation [5, 6]. The PBE describes the time evolution of the NDF in the real space (position) and in the phase space determined by the chosen internal coordinates for the description of the NDF (size, velocity, temperature...). Simulating the PBE can be achieved by using the Lagrangian direct simulation Monte-Carlo method (DSMC [7]), which solves Lagrangian equations for a large sample of particles, in order to reach converged statistics. This approach is considered as the most accurate, but is very expensive, especially for unsteady flows, and is not well adapted for high performance parallel computing (load balancing [8]) as well as for coupling to the gas phase (interpolations between gas and disperse phases [8]). Its use for industrial applications stays unreachable, even with the great increase in computational resources. Eulerian methods can overcome this problem by not directly solving the PBE on the NDF, but its moments, which are integrated quantities over phase space. In idealized cases of monodisperse distributions, i.e. a unique size for all droplets, the NDF can be easily reconstructed because only two moments are necessary to uniquely determine it. But in the case of polydisperse distributions, a finite moment set has potentially an infinity of admissible NDF reconstructions, which is called the Hausdorff moment problem [9], and the goal is to be able to determine a unique NDF, by imposing additional constraints on the reconstruction.

To account for the size polydispersity, three ways can be envisaged:

1. A size space discretization: the size space can be discretized into intervals called "sections" [10], which leads to a Finite Volume formulation called Multifluid approach in the context of sprays [11].
2. A quadrature-based moment method : a set of moments is used to build a quadrature approximation of the NDF [12, 13].
3. A moment method with continuous reconstruction: a limited set of size moments is used to reconstruct the NDF [14, 15].

Discretizing the size phase space is the simplest way to capture the size polydispersity, but in order to limit diffusion in size space, a high number of sections is needed, thus increasing the computational cost [16]. Adopting a moment point of view may overcome this problem by transporting only one "fluid" with several moments. This can be done using QMOM (quadrature method of moment) [12] or DQMOM (direct quadrature method of moment) [13]. Those approaches are linked by the reconstruction of the NDF : a sum of Dirac δ-functions evolving jointly. The difference lies on the fact that QMOM solves equations on the moment set, whereas DQMOM directly solves the equation on the weight and abscissas of the Dirac δ-functions. Those two methods had shown their great potential for coalescence or breakage, but encounter difficulties for evaporating spray, especially with continuous distributions, due to the disappearance flux of droplets at zero size [17]. Actually, the lower order representation of the QMOM or the DQMOM is not able to reproduce this continuous flux, the disappearance of droplet being possible only when a Dirac delta function reaches the zero abscissa, and leading to singular fluxes.

To solve this intrinsic problem of the representation of the NDF, Kah et al. [2, 15] have proposed a new strategy, called Eulerian Multi-Size Moment model (EMSM), taking advantage of a continuous description of the NDF to determine the flux at zero size, and the evaluation of the shift in size induced by evaporation by a combined flux/quadrature approach. The reconstruction of the NDF is done by Entropy Maximization (EM) [18]. This is a convex optimization problem with constraints, which admits a unique solution, as long as the moment vector stays in the interior of the moment space [19]. This NDF is used to compute the flux at zero size, and the evaporation is evaluated by means of the zero flux and a quadrature approximation. The great potential of EMSM is demonstrated in [20], where it is shown that the computational time for a equivalent accuracy is clearly an advantage over the Multifluid method.

The evolution in size phase space solved, an important issue to be tackled concerns the numerical scheme used to transport the set of moments in the physical space. In general, a first order Finite Volume scheme is able to transport a set of moments vector, preserving the moment space. But for complex problems, high order methods are needed. As shown in [21], classical high order finite volume numerical schemes cannot guaranty to keep the moments in the interior of the moment space. To overcome this difficulty, a kinetic scheme adapted to a high number of moments is proposed in [20], which uses a linear reconstruction on the canonical moments, and preserves the realisability of the moment set.

The EMSM associated with a stable and realizable kinetic scheme for the physical transport is a good candidate for the simulation of complex flows and has already been implemented in industrial code such as IFP-C3D [22, 23]. But two important issues still remain unsolved. Firstly, the EMSM uses the same velocity for all droplets, independently of their size. This is quite a strong assumption when drag force is accounted for, as it may generate size-conditionned differential dynamics. The effect of such an assumption is illustrated in Fig. 1, which consists in the injection of droplet perpendicularly to a gaseous crossflow at constant and uniform velocity, with a constant size distribution for which Stokes number based on the convective time of the gas phase ranges in $[0.083, 0.744]$. When only one velocity is considered for the whole distribution, only one trajectory can be reproduced. This effect is partially accounted for, using a Multifluid approach with 10 sections, because each section has its proper velocity. But for a coarse size discretization, this leads to distinct trajectories separated by vacuum regions, as in Fig. 1. Secondly, the ability to capture separated dynamics depending on the droplet size would generate quasi-monodisperse distributions. Unfortunately, the EMSM and its related EM algorithm encounter difficulty in reproducing this kind of NDF, which are close to the frontier of the moment space. This limits the applicability of the EM or at least introduces an error for NDF close to the frontier [15]. This type of highly segregative flows is typical of swirling injection [14] in aeronautical configurations, even if the turbulent mixing tends to generate continuous and regular NDF.

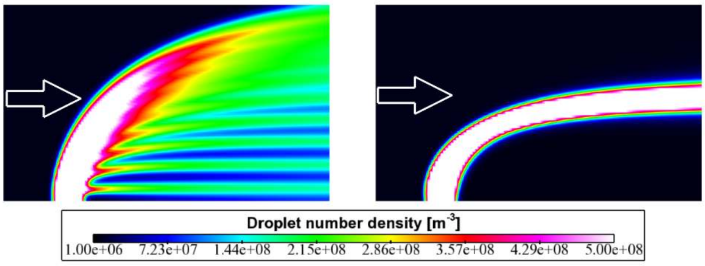

Figure 1: 2D Crossflow: Multifluid method with 10 sections (left) and EMSM equivalent to a monodisperse-monokinetic approach in this non-evaporating case (right). Stokes numbers are in the range $[0.083, 0.744]$ for the Multifluid method and 0.332 for the EMSM approach.

In this work, the aim is to propose a modelling and numerical framework adapted to address these two issues. The entropy maximization and its algorithms are enhanced using adaptive procedures, in terms of integration methods and controlled moments, and tabulated initial guess. A new method is proposed, called Coupled Size-Velocity Moments model (CSVM) that takes into account size-velocity correlations by the transport of an additional size-velocity moment for each space dimension, which permits to reconstruct the velocity against size. The evolution in size space for the size moments is done by the determination of the disappearance flux of droplets coupled to a size quadrature approximation. But, contrary to the initial EMSM where the evolution of velocity moments is straightforward due to the a unique velocity for all sizes, the newly introduced size-velocity moments also evolve in size space using both size and velocity reconstructions. The evolution in velocity space due to drag force is done using a CQMOM quadrature [24] coupled to EMSM, which permits to account for the coupled size and velocity evolution, by integrating ordinary differential equations. Using a quadrature approach for the evolution in phase space is important, because complex laws for drag force, evaporation and heating can be easily accounted for, even if we consider simple laws in this work [15]. This new moment method is then assessed in 0D for both evaporating and non-evaporating cases and is shown to capture size-conditioned dynamics even in the configuration of oscillating gaseous flow field and in the presence of a large spectrum of sizes. A new numerical kinetic scheme is introduced for the convection in real space, which is based on the flux splitting technique, and preserves the moment space. This transport scheme is evaluated in 1D cases, its order studied and its robustness demonstrated. We then switch to two extreme non-evaporating cases in order to isolate the size-velocity correlations due to drag force and convection, the evaporation part having already been characterized in the framework of EMSM studies [15, 20]. We study a crossflow case and a Taylor-Green case, with steady gaseous velocity fields, where a strong size-conditioned dynamics leads to moment vectors very close the frontier of the moment space. Comparisons with either analytical solutions or other solvers such as Lagrangian, Multifluid or EMSM show the potential and the accuracy of the method. Eventually, in order to provide a test-case closer to more realistic unsteady configurations, we investigate a weakly turbulent free jet with a very large size spectrum in a non-evaporating configuration. An excellent agreement is obtained compared to Lagrangian and Multifluid with 10 sections, thus completing the assessment of the method. We finally provide comments on the memory storage and computational cost of the method as well as on its application to industrial configurations and potential extensions.

The paper is organized as follows. First, the EMSM is described, with its advantages and drawbacks in Section 2. Then improvements of the EM are presented in Section 3, in order to be able to reproduce the whole moment space within a controlled error. The CSVM which takes into account size-velocity correlations is introduced in Section 4. Concerning the evolution in phase space and the transport in physical space, the drag/evaporation strategy and the flux splitting kinetic scheme are detailed and evaluated on 0D/1D cases in section 5. Finally, an evaluation in 2D extreme cases of crossflow and Taylor-Green vortices is investigated in section 6 as well as the final free jet configuration.

2. The Eulerian Multi-Size Moment model

2.1. The moment problem

We consider dilute sprays at high Knudsen numbers, so that collisions are negligible and there is no effect of the dispersed phase on the gas phase. The phase space of the NDF is limited to size S and velocity v in one dimension, leading to the following PBE:

$$\frac{\partial f}{\partial t} + v\frac{\partial f}{\partial x} + \frac{\partial}{\partial v}\left(\frac{v - u_g}{\tau_p} f\right) + \frac{\partial R_S f}{\partial S} = 0, \tag{1}$$

where $R_S = \mathrm{d}S/\mathrm{d}t$ is the evaporation rate which is constant in the case of d^2 evaporation laws and τ_p the relaxation time of the droplets for Stokes drag. Using non-dimensional variable $S^* = S/S_{max}$, $t^* = t/\tau_g$, $v^* = v/v_{ref}$ where S_{max} is the maximum droplet surface, τ_g and v_{ref} a reference time scale and velocity of the gaseous flow, we obtain the non-dimensional PBE:

$$\frac{\partial f}{\partial t^*} + v^*\frac{\partial f}{\partial x^*} + \frac{\partial}{\partial v^*}\left(\frac{v^* - u_g^*}{\mathrm{St}} f\right) + \frac{\partial R_S^* f}{\partial S^*} = 0, \tag{2}$$

where $\mathrm{St} = \tau_p/\tau_g$ is the Stokes number. For sake of clarity, star exponent will be dropped for non-dimensional variables. To solve this equation, we are looking at the moments of the NDF. In one dimension, these are defined by:

$$M_i^l(t,x) = \int_{-\infty}^{\infty}\int_0^1 S^l v^i f(t,x,v,S)\mathrm{d}v\mathrm{d}S. \tag{3}$$

The equation for $M_i^l(t,x)$ is then:

$$\begin{aligned}\frac{\partial M_i^l}{\partial t} + \frac{\partial M_{i+1}^l}{\partial x} \quad = \quad & -\int_0^1 i\frac{S^l}{\mathrm{St}}\left(v^i - u_g v^{i-1}\right) f\mathrm{d}S\mathrm{d}v \\ & + R_S M_i^{l-1} + R_S\left[\int_{-\infty}^{\infty} v^i S^l f(t,x,v,S)\mathrm{d}v\right]_{S=0}^{S=1}.\end{aligned} \tag{4}$$

In this equation, the main issues concern the modelling of the second left hand side term (convection) and the third right hand side term (evaporation). The former is due to the fact that with a finite set of moments, the flux for the highest order moment equation is unclosed. The latter imposes the knowledge of point-wise values of the NDF at the edge of the size phase space.

2.2. The moment space

Even if the moment space where lies the size moment vector $\mathcal{M}_0 = (M_0^0, M_0^1, ..., M_0^N)$ is convex, it has a complex geometry in the semi-open space $\mathbb{R}_+^{N+1}$ [15]. The normalized moments vector $(M_0^1/M_0^0, ..., M_0^N/M_0^0)$ lives in a closed convex space of $[0,1]^N$, but still has a complex geometry. A simpler space can be determined by using the canonical moments [19]. The first four canonical moments are:

$$\begin{aligned} p_0 &= 1, & (5)\\ p_1 &= \frac{M_0^1}{M_0^0}, & (6)\\ p_2 &= \frac{M_0^0 M_0^2 - (M_0^1)^2}{M_0^1(M_0^0 - M_0^1)}, & (7)\\ p_3 &= \frac{(M_0^0 - M_0^1)(M_0^1 M_0^3 - (M_0^2)^2)}{(M_0^0 M_0^2 - {M_0^1}^2)(M_0^1 - M_0^2)}. & (8) \end{aligned}$$

So the actual moments reads:

$$\begin{aligned} M_0^1 &= M_0^0 p_1, & (9)\\ M_0^2 &= M_0^0 p_1 \left[(1-p_1)p_2 + p_1\right], & (10)\\ M_0^3 &= M_0^0 p_1 \left[(1-p_1)(1-p_2)p_2 p_3 + \left[(1-p_1)p_2 + p_1\right]^2\right]. & (11) \end{aligned}$$

The canonical moments live in the full cube $[0,1]^N$, leading to simpler analysis, especially in terms of realisability of the moment vector. The frontier of the moment space is defined by values 0 or 1 for a canonical moment p_k, and implies that canonical moments of order greated than k are not defined. This frontier is characterized by the existence of a unique solution for the NDF, a sum of weighted Dirac δ-functions. In the interior of the moment space where canonical moments are neither equal to 0 nor 1, there is an infinity of NDF, the moments of which are a finite moment vector.

The EMSM tackles the problem of evaporation terms by a reconstruction of the NDF. In this work we will considered 4 moments in size, but the method can be extended to more moments. Considering the velocity does not depend on the size, the NDF can be decomposed in the following way:

$$f(t,x,v,S) = n(t,x,S)\delta(v - U(t,x)), \tag{12}$$

where $U = M_1^0/M_0^0$. The EMSM reconstructs $n(t,x,S)$ using Entropy Maximization (EM)[18]. The Shannon Entropy is defined by:

$$\mathbf{H}(f) = -\int_0^1 n(t,x,S)\ln n(t,x,S)\mathrm{d}S. \tag{13}$$

Associated with N moments constraints, the maximization of $\mathbf{H}(f)$ imposes the unique following reconstruction:

$$n(S) = \exp\left(-\sum_{j=0}^{N} \zeta_j S^j\right), \tag{14}$$

where ζ_j are Lagrange multipliers. The following convex potential is then minimized:

$$\Delta = \int_0^1 \left[\exp\left(-\sum_{j=0}^{N} \zeta_j S^j\right) - 1\right] \mathrm{d}S + \sum_{j=0}^{N} \zeta_j M_0^j. \tag{15}$$

Indeed, its stationary points are given by:

$$\frac{\partial \Delta}{\partial \zeta_i} = 0 \Rightarrow \int_{S_{min}}^{S_{max}} S^i \exp\left(-\sum_{j=0}^{N} \zeta_j S^j\right) \mathrm{d}S = M_0^i. \tag{16}$$

Numerically, this non-linear system is solved using a Newton method: starting form initial choices $\zeta = (\zeta_0, ..., \zeta_N)^T$, updated ζ is defined from:

$$\zeta^+ = \zeta - H^{-1}(\mathcal{M}_0 - \langle X \rangle_\zeta), \tag{17}$$

where $\langle X \rangle_\zeta = (\langle x^0 \rangle_\zeta, ..., \langle x^N \rangle_\zeta)^T$ is the vector of approximated moments:

$$\left\langle x^i \right\rangle = \int_0^1 x^i \exp\left(-\sum_{j=0}^{N} \zeta_j x^j\right) dx, \tag{18}$$

and H is the Hessian matrix defined by $H_{i,j} = \frac{\partial \Delta}{\partial \zeta_i \partial \zeta_j} = \left\langle x^{i+j} \right\rangle_\zeta$ for $i, j = 0, .., N$. Higher order moments are computed using an integration by parts [25]:

$$\left\langle x^{N+k} \right\rangle = \frac{1}{N \zeta_N} \left((k+1) \langle x \rangle^k - \sum_{l=1}^{N-1} l \zeta_l \langle x \rangle^{l+k} + W_k(1, \zeta) - W_k(0, \zeta) \right), \tag{19}$$

where $W_k(a, \zeta) = a^{k+1} \exp(-\sum_{j=0}^{N} \zeta_j a^j)$. A Gauss-Legendre quadrature method evaluates the integrals. In [15], it has be proven that this integration method with 24 quadrature points is sufficient to reach the subset $[0.01, 0.99]^3$ of the canonical moment space and that it is sufficient to evaluate the disappearance flux of droplet at zero size within an error less than 1%.

Starting from the reconstructed NDF, The evaluation of the evaporation process is made in two steps. First, the disappearance flux at zero size is evaluated, and corresponds to the part of the moment that will disappear during a time step Δt:

$$F_i^l = \int_0^{R_S \Delta t} U^i S^l n_l(S) \mathrm{d}S. \tag{20}$$

The moments are then corrected:

$$\tilde{M}_i^l = M_i^l - F_i^l. \tag{21}$$

The evolution in phase space is determined by a quadrature approach:

$$\begin{aligned} \tilde{M}_i^l &= U^i \sum_{k=1}^{2} w_k S_k^l, && (22) \\ \frac{dS_k}{dt} &= R_S, && (23) \\ S_k(t + \Delta t) &= S_k(t) + R_S \Delta t. && (24) \end{aligned}$$

As stated in [15], this method can account for d^2-law as well as arbitrary evaporation law with a good accuracy.

For the transport in physical space, Kah et al. [20] developed a second order Finite Volume scheme based on a spatial reconstruction of the canonical moments, which preserves the moment space. The authors evaluated the full strategy on complex 2D configurations and have proven its ability to predict such evaporating polydisperse flows, as well as its high efficiency comparing to the Multifluid approach.

3. Numerical issues with Entropy Maximization

In [15], the Entropy Maximization is used to quantify the disappearance flux of droplets. Such an algorithm was designed in order to mainly treat smooth distribution where the EM reconstruction associated with a Gauss-Legendre quadrature is able to reach a controlled precision of typically 10^{-6} on the evaporative flux, within the limit of a reasonable number of Newton steps. Even if some treatment was proposed in [15] at the frontier of the moment space, the method could only achieve a precision of 10^{-2} on the moments in the favorable context of size-velocity decoupling which was coherent with the expected level of modelling of that paper. Unfortunately, in the present context, where we reach a much better precision in terms of size-velocity coupling and treatment of polydispersion, the frontier of the moment space will have a much more important role and we need to upgrade such a EM procedure in both precision and algorithmic efficiency in order to cope up with the increase of modelling level.

Three new ingredients will be introduced in the present section. First, in order to drastically increase the computational efficiency of the EM subroutine, a tabulated initial guess for the Newton solver has been implemented and we provide the key features of such an approach which is used in most of the interior of the moment space, that is in the cube $[0.1, 0.9]^3$ in terms of the canonical moments. Second, two ingredients will be added in order to cope with a large subset of the moment space close to the frontier. An adaptive support for the evaluation of the integrals in the EM subroutine has been implemented, thus leading to an important gain in precision. Besides, an adaptive reduction of the number of parameters required for the description of the moments vectors very close to the frontier of the moment space is implemented, which allows to further the same level of precision much closer to the frontier of the moment space than it was achieved in [15]. These improvements will prove to be exactly what is needed as far as an accurate description of the moment space, in order to cope with a precise description of the size-velocity correlations.

3.1. Tabulation

To reduce the number of iterations needed for the Newton solver to converge, the tabulation of all parameters is considered. The evolution of the parameters against canonical moments is first investigated. In Fig. 2, parameters ζ_1, ζ_2 and ζ_3 of the behaviour are plotted against p_2 and p_3 for $p_1 = 0.1, 0.5, 0.9$. Notice that p_2 and p_3 vary between 0.1 and 0.9. Considering the smooth evolution of parameters in the interior of the moment space, the tabulation may give accurate results. The question is now to evaluate the error for a direct tabulation of the parameters.

Two interpolation methods are compared for the tabulation: a linear reconstruction and a third order polynomial reconstruction. The tabulation step is $\Delta p = 0.01$ for each canonical moment, and the tabulation is done in the cube $[0.1, 0.9]^3$.

On Tab. 1, the error made on the moments by the two methods are compared for different sets of canonical moments in the interior of the moment space. Each set is chosen to be as far as possible from tabulated values, to exhibit the maximal error. It can be seen that with a third order polynomial the error can be close to 10^{-4}, which could be sufficient depending on the needed accuracy.

p_1	p_2	p_3	Linear	3rd order
0.105	0.105	0.105	3.8e-3	7.0e-5
0.505	0.505	0.505	3.3e-4	2.9e-7
0.895	0.895	0.895	3.7e-3	1.0e-4
0.505	0.105	0.105	4.3e-3	4.8e-5
0.505	0.895	0.895	2.6e-3	7.3e-5

Table 1: Error on moments using a linear or a third order interpolation method for five sets of canonical moments.

If a higher precision is required, it is proposed to use the tabulation to define an initial guess for the Newton iterative solver, which is supposed to reduce the computational time needed to reach a given accuracy of 10^{-6}. On Tab. 2, it can be seen that the tabulation of the initial guess lowers significantly

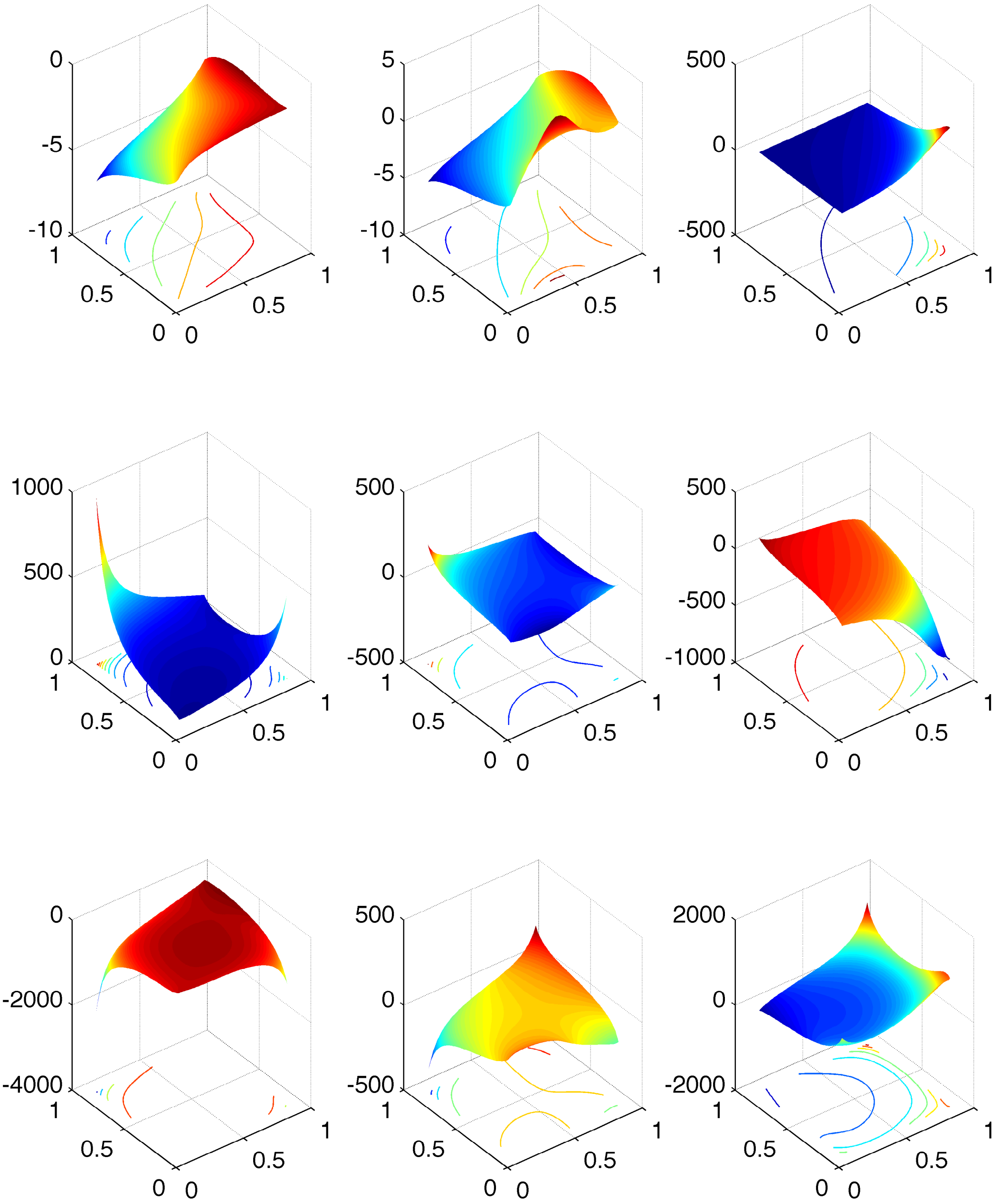

Figure 2: Entropy maximization parameters: ζ_1(up), ζ_2(center) and ζ_3(down) against canonical moments p_2 and p_3, with $p_1 = 0.1$ (left), $p_1 = 0.5$ (center), $p_1 = 0.9$ (right).

the computational time and the number of Newton iterations needed, the fastest method being the more precise third order reconstruction for the initial guess.

p_1	p_2	p_3	Constant	Nearest	Linear	3rd order
0.105	0.105	0.105	1.18s/12it	0.55s/4it	0.33s/2it	0.25s/1it
0.505	0.505	0.505	0.27s/4it	0.18s/2it	0.12s/1it	0.09s/0it
0.895	0.895	0.895	5.13s/17it	0.81s/3it	0.61s/2it	0.43s/1it
0.505	0.105	0.105	1.35s/8it	0.69s/3it	0.52s/2it	0.37s/1it
0.505	0.895	0.895	1.91s/10it	0.69s/3it	0.54s/2it	0.38s/1it

Table 2: Computational time and number of iterations using a constant initial guess, or a tabulated initial guess with nearest point, with linear or third order interpolation method for five set of canonical moments.

3.2. Dealing with the frontier of the moment space

As stated in the previous section, the parameters ζ evolves slowly with the canonical moments in the subspace $[0.1, 0.9]^3$. But close to the frontier, where at least one canonical moment is in $[0.0, 0.1] \cup [0.9, 1.0]$, the variation of ζ for a small variation of the canonical moments could be very important. The tabulation technique cannot be used in this part of the moment space. However the initial guess for the Newton solver is chosen to be the closest point in $[0.1, 0.9]^3$. Now being closer to this frontier imposes two constraints on the Newton solver used for EM: NDF becomes singular, and the determinant of the Jacobian matrix becomes close to zero, leading to ill-conditioned matrices. We thus introduce two strategies to handle the frontier of the moment space: an adaptive support for the integrals and a way to choose the optimal number of entropy maximization parameters.

3.2.1. Adaptive support for the integrals

The reconstruction can exhibit very high variations for limiting cases near the frontier of the moment space. In such cases, the classical Gauss Legendre quadrature may use abscissas where the function is close to zero, limiting the precision of the method. To overcome this problem, an adaptative support for the gaussian quadrature is proposed. This support is set for a given threshold ϵ_0 in order to locate zones with negligible number density:

$$\exp\left(\sum_{j=0}^{N} \zeta_j S^j\right) = \epsilon_0, \tag{25}$$

$$\sum_{j=0}^{N} \zeta_j S^j - \ln \epsilon_0 = 0. \tag{26}$$

Finding the roots of this polynomial allows to define the integration intervals. As we considered four size moments in this work, the integration support will be made of one or two intervals (as the polynomial will have 3 real roots at most). In practice ϵ_0 is set to the expected tolerance on the integrals evaluation (to reach an accuracy of ϵ on the integrals, ϵ_0 is set to ϵ).

The ability of the adaptive support to compute the integral of singular functions is assessed on the computation of the integral of $\exp(-KS)$ for which the analytical solution is easily found. In Fig. 3, the relative error made by both fixed and adaptive support Gauss Legendre integration methods are shown. For $n(S) = \exp(-10S)$, the two methods exhibit the same results, as the function extremum on the interval are not so far ($n(S = 0) = 1$ and $n(S = 1) = \exp(-10) = 4.5.10^{-5}$), and the support stays $[0, 1]$ for the adaptive method. For $n(S) = \exp(-10^2 S)$, the adaptive support is activated, as the extremum values are 1 at $S = 0$ and $n(S = 1) = \exp(-10^2) = 3.7.10^{-44}$. With a threshold at 5.10^{-6}, the adapted support is now $[0, 0.398]$ and the accuracy of the adaptive method is considerably higher, even if the fixed support method is able to compute this integrals with high but reasonable number of nodes. For $n(S) = \exp(-10^4 S)$, the

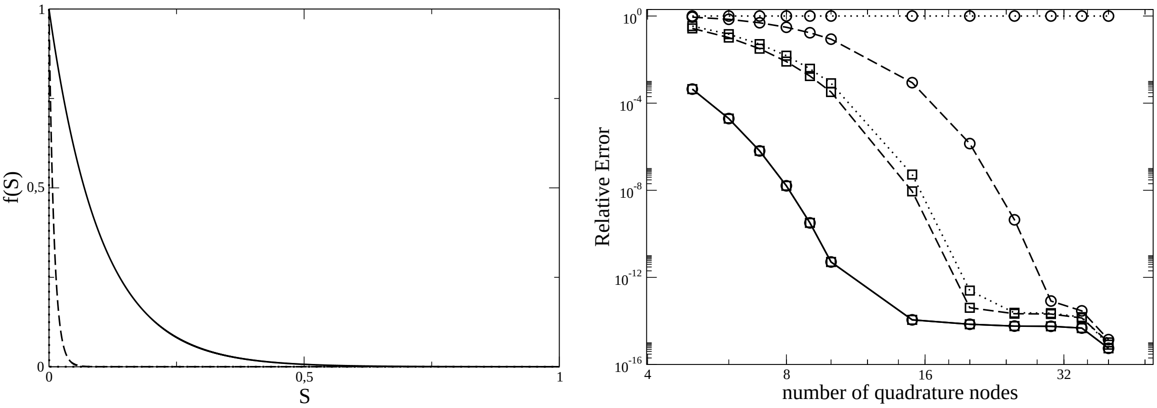

Figure 3: Adaptive integrals: (left) Function $f(S) = \exp(-KS)$ for $K = 10^1$ (full line), $K = 10^2$ (dashed line) and $K = 10^4$ (dot-dashed line) and (right) relative error on the integrals with fixed (circle) and adaptive (square) supports.

fixed support method is not able to compute this integral, even with 40 nodes, where the adaptive method uses the support $[0, 4.44.10^{-3}]$ and computes the integral within an error less than 10^{-6} with only 15 nodes, and confirms the importance and the accuracy of the proposed integration method.

3.2.2. Reduction of the number of parameters at the frontier of the moment space

At the frontier of the moment space, the distribution is close to a sum of Dirac δ-functions. For a four-moments reconstruction the limit case is a δ-function in $]0, 1[$, possibly with a δ-functions at $S = 0$ or $S = 1$, which can be uniquely determined by only three moments. So it appears that close to the frontier, less moments are needed to capture the NDF. The idea here is to determine where using less than four moments is effective in the sense that we reach the same level of accuracy without leading to unstable numerical methods. The introduced error has to be controlled, as only the frontier is uniquely determined by less moments.

One can notice that each moment linearly depends on the canonical moment of the same order. So, with respect to p_k, the moment m_k is bounded between ${M_0^k}^{min} = M_0^k(p_k = 0)$ and ${M_0^k}^{max} = M_0^k(p_k = 1)$. The distance between minimum and maximum values is then:

$$\delta M_0^k = \frac{M_0^k(p_k = 1) - M_0^k(p_k = 0)}{M_0^0}. \tag{27}$$

So if M_0^3 is considered (here the highest order moment):

$$\delta M_0^3 = p_1 p_2 (1 - p_1)(1 - p_2). \tag{28}$$

When this distance is close to 0, the moment M_0^3 weakly depends on p_3, which says that the moment M_0^3 can be accurately reproduced with the first three moments only. The subset where controlling the first three moments is sufficient to achieve an accuracy $\epsilon_3 = 10^{-3}$ on M_0^3 is represented on Fig. 4. When the moment vector is closer to the frontier of the moment space than this limit, the number of controlled moment is reduced from 4 to 3.

The same procedure can be applied to reduce from 3 to 2 moments using the normalized distance for M_0^2:

$$\delta M_0^2 = p_1(1 - p_1), \tag{29}$$

which gives that if this distance is close to zero the number of controlled moments can be reduced from 3 to 2. This condition being more restrictive than the one on δM_0^3, fulfilling it will be sufficient to reduce from 4 to 2 controlled moments.

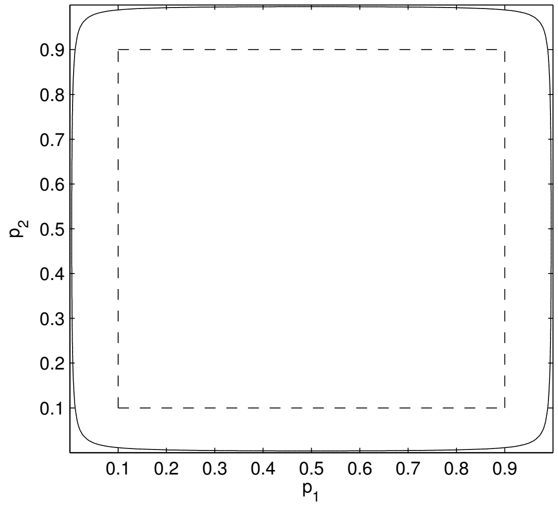

Figure 4: Subsets of the moment space where tabulation and reduction of controlled moments are used against p_1 and p_2: limit within the tabulation is envisaged with a tolerance of 10^{-4} (dashed line) and limit within 3 size moments are sufficient to achieve a precision of 10^{-3} on M_0^3 (solid line).

3.3. Conclusions on the entropy maximization

The proposed adaptive support for integrals enables the accurate computation of the integrals of almost singular NDF. With the knowledge of the canonical moments, we are now able to choose an optimal initial guess for the Newton solver by means of a tabulation. The number of moments used for the reconstruction can be reduced where less moments are needed. This reduction is limited to a subspace close to the frontier, and we are able to define precisely the error made by this reduction of parameter.

So the EM is now able to reproduce a large subset of the moment space, and is ready for highly segregative cases like the crossflow (Fig. 1), where the drag force separates the droplets into quasi-monodisperse NDF, which correspond to moment vectors lying at the frontier of the moment space.

4. Accounting for size-velocity correlation: the CSVM method

4.1. Description of the problem

The initial EMSM considers a unique velocity for all sizes. In moderate to high Stokes flows, the velocity of each size would be different, as exhibited in Fig. 1 in the crossflow configuration. So the NDF now writes:

$$f(t,x,v,S) = n(t,x,S)\delta(v - U(t,x,S)), \tag{30}$$

where U depends on position and time, but also on droplet surface. To describe this velocity distribution, a reconstruction strategy is proposed. The starting point is the same as the initial EMSM for the reconstruction of the size distribution: with a certain number of moments, we need to have an accurate enough description of the NDF. As we want to build size-velocity informations, size-velocity moments will be used so that the CSVM will use size moments to determine the size distribution $n(S)$ and size-velocity moments to determine $U(S)$. As the determination of $n(S)$ does not need $U(S)$ (size moments does not depend on $U(S)$), this first step of the EMSM is unchanged. However the velocity reconstruction depends on the size reconstruction.

4.2. Strategy for the velocity reconstruction

Hereafter, the reconstruction strategy for one dimension is proposed. The application for others directions is straightforward, as the used size-velocity moments will be at first order in velocity ($i = 1$):

$$M_i^l = \int_0^1 S^l U(S)^i n(S) \mathrm{d}S. \tag{31}$$

To evaluate the velocity of each size, a reconstruction shape of $U(t, x, S)$ is proposed. A constraint on this reconstruction is that droplets with a null size and so a null relaxation time follow the gas phase:

$$U(t, x, S = 0) = u_g. \tag{32}$$

To be able to represent all possible moment vectors, it is necessary to propose a reconstruction that can describe the full velocity moment space. The following power reconstruction is proposed:

$$U(t, x, S) = u_g + \sum_{k=1}^{N} A_k S^{\alpha_k}, \tag{33}$$

where A_k are the parameters used to control the size-velocity moments, and α_k are user-determined with $\alpha_1 < \alpha_2 < ... < \alpha_N$. Considering size-velocity moments expression, one can write:

$$M_1^l = M_0^l u_g + \sum_{k=1}^{N} A_k \int_0^1 S^{\alpha_k + l} n_l(S) \mathrm{d}S, \tag{34}$$

which gives the linear system for the parameters vector $\mathcal{A}$:

$$P\mathcal{A} = \mathcal{N}, \tag{35}$$

where:

$$\begin{aligned} P_{kl} &= \int_0^1 S^{\alpha_k + l} n_l(S) \mathrm{d}S, \\ N_l &= M_1^l - M_0^l u_g. \end{aligned}$$

Considering the linear system, the only configuration for which this reconstruction will not be possible for a given moment vector corresponds to the zero determinant for matrix P. This condition is reached for a Dirac's δ-function for the size distribution $n(S)$. As the EM does not generate this type of distribution, our reconstruction strategy can reproduce any moment vector given by the proposed method.

In [14], an exponential reconstruction is proposed, based on the analytical solution of the relaxation of droplets at constant gas velocity. Although this is a physical and relatively smooth reconstruction, with good asymptotic predictions, this shape is not able to reproduce all the moment space, as it cannot capture inversions in the relative velocity between gas and droplets, which is a typical case with oscillating gas velocity. In this work, as the aim is to design a method with as few moments as possible, only one additional size-velocity moment per dimension will be used, compared to the original EMSM.

4.3. Evaluation of the proposed strategy

To evaluate the proposed reconstruction, a 0D analytical test case is proposed, in which an initial size-velocity distribution evolves because of the drag force imposed by a constant gas velocity. The initial size and velocity distributions are constant so that $n(S, t) = 1$ and $U(S, t = 0) = U^0$. For each size, this case is solution of the ordinary differential equation:

$$\frac{\mathrm{d}U(S, t)}{\mathrm{d}t} = -\frac{U(S, t) - u_g}{\mathrm{St}(S)}, \tag{36}$$

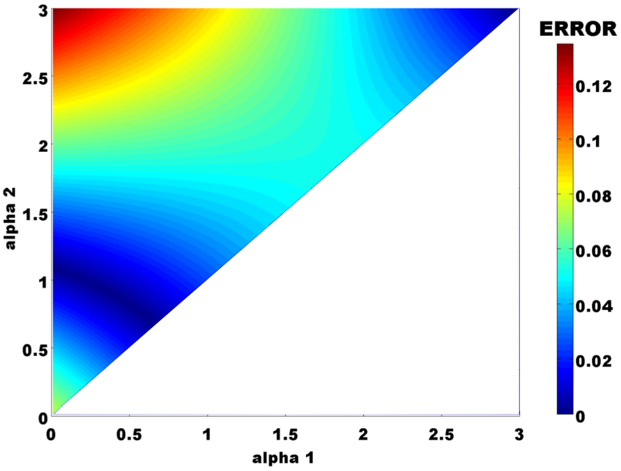

Figure 5: CSVM reconstruction error for the 0D test case at constant gas velocity for $t = 1$ against α_1 and α_2. For $\alpha_2 < \alpha_1$ the error is not plotted. For $\alpha_1 = \alpha_2$, the reconstruction is undefined.

so:

$$U(S,t) = u_g + (U^0 - u_g)\exp\left(-\frac{t}{\mathrm{St}(S)}\right). \tag{37}$$

The moments evolution against time is:

$$\begin{aligned} M_1^l(t) &= \int_0^1 S^l U(S,t) n(S)\mathrm{d}S = \frac{u_g}{l+1} + (U^0 - u_g)\int_0^1 S^l \exp\left(-\frac{t}{\mathrm{St}(S)}\right)\mathrm{d}S, && (38)\\ M_1^0(t) &= u_g + \frac{t}{K_d}(U^0 - u_g)\Gamma_{inc}\left(-1, \frac{t}{K_d}\right), && (39)\\ M_1^1(t) &= \frac{u_g}{2} + \frac{t^2}{K_d^2}(U^0 - u_g)\Gamma_{inc}\left(-2, \frac{t}{K_d}\right), && (40)\end{aligned}$$

where $\Gamma_{inc}(a,z) = \int_z^\infty x^{a-1}\exp(-x)\mathrm{d}x$ is the upper incomplete gamma function and $\mathrm{St}(S) = K_d S$, which corresponds to Stokes drag.

In Fig. 5, the influence of the power α_1 and α_2 on the absolute reconstruction error in L^∞ norm is shown for $t = 1$. Two optimal zones are exhibited, the first one with high powers nearly identical, and the second one with one power close to 1 and the second one less than 1. In practice, $\alpha_1 = 0.5$ and $\alpha_2 = 1$ will be used.

Results are plotted in Fig. 6. For a two parameters reconstruction, it proves to be efficient except for a constant velocity distribution, which artificially breaks the assumption $U(S = 0) = u_g$.

A second analytical test case is proposed, with variable gas velocity $u_g = \alpha\cos(\beta t)$. It aims at representing the velocity profile inside a vortex, and so the effect of a turbulent structure. The solution of Eq. 36 is then:

$$U(S,t) = \frac{\alpha\left(\beta \mathrm{St}\sin(\beta t) + \cos(\beta t)\right)}{\beta^2\mathrm{St}^2 + 1} + \frac{\left[U^0\beta^2\mathrm{St}^2 + (U^0 - \alpha)\right]\exp\left(-\frac{t}{\mathrm{St}}\right)}{\beta^2\mathrm{St}^2 + 1}. \tag{41}$$

Results are plotted in Fig. 7. Again the reconstruction is satisfactory with only two moments and so two parameters, and proves to be able to reproduce distributions with an inversion of the gas relative velocity, which would be typical of turbulent flow with a wide spectrum of droplet sizes. Furthermore, as a relative velocity inversion occurs, an exponential function would not be able to reproduce such a distribution.

So we are able to reconstruct the droplet number density as well as the velocity for each size. Now, we need to predict the evolution of this NDF through evaporation, drag force and convection.

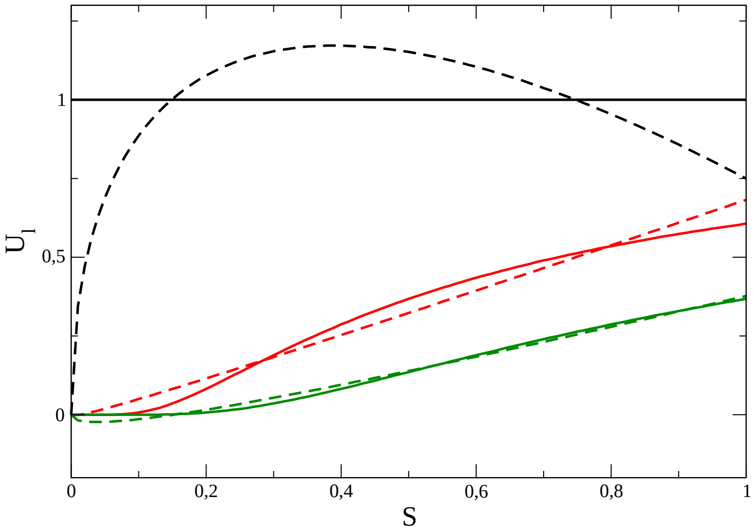

Figure 6: 0D analytical test case with constant gas velocity: velocity distribution (solid lines) and its reconstruction by CSVM (dashed lines).

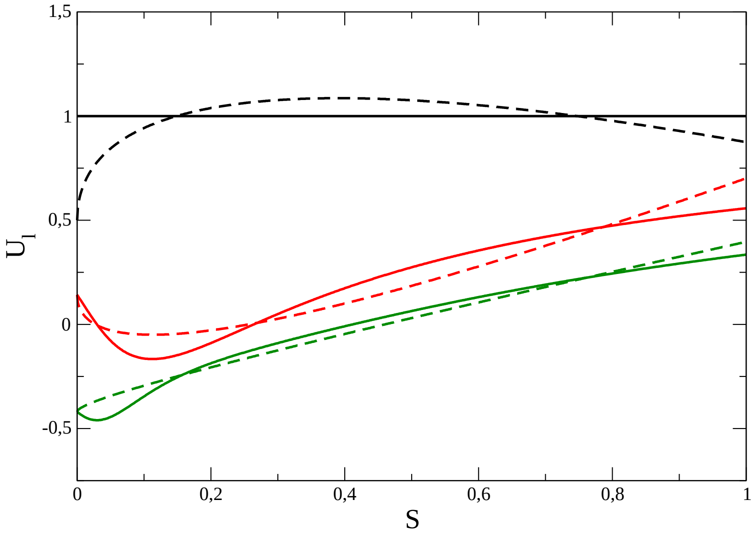

Figure 7: 0D analytical test case with sinusoidal gas velocity: velocity distribution (solid lines) and its reconstruction by CSVM (dashed lines).

5. Numerical methods for the moment evolution

5.1. Evaporation and drag force

5.1.1. Description of the proposed strategy

We present a new strategy for the evolution of the NDF through evaporation and drag force. Whereas the method described in [15] is based on two main steps: the evaluation of the disappearance flux of droplet, and the evolution in size space, the strategy is here extended to the evolution in velocity space through drag force. First the derivation is shown for d^2 law and Stokes drag ($R_S = cte$ and $\mathrm{St}(S) = K_d S$). The size reconstruction of the CSVM enables the computation of the disappearance flux of droplet F_i^l for each moment and for one time step Δt:

$$F_i^l = \int_0^{-R_S \Delta t} U(S)^i S^l n_l(S) \mathrm{d}S, \tag{42}$$

corresponding to the part of the distribution which reaches the zero size during one time step. The moment are then corrected:

$$\tilde{M}_i^l = M_i^l - F_i^l. \tag{43}$$

The evolution in phase space is determined by a CQMOM-like quadrature approach [24] :

$$\begin{aligned} \tilde{M}_i^l &= \sum_{k=1}^{2} w_k S_k^l U_k^i, & (44)\\ \frac{\mathrm{d}U_k}{\mathrm{d}t} &= -\frac{1}{\mathrm{St}}\left(U_k - u_g\right) = -\frac{1}{K_d S_k}\left(U_k - u_g\right), & (45)\\ \frac{\mathrm{d}S_k}{\mathrm{d}t} &= R_S. & (46) \end{aligned}$$

The size and velocity after one time step is:

$$\begin{aligned} S_k(t+\Delta t) &= S_k(t) + R_S \Delta t, & (47)\\ U_k(t+\Delta t) &= \left(U_k(t) - u_g(t)\right)\left(\frac{S_k(t) + R_S\Delta t}{S_k(t)}\right)^{\frac{-1}{K_d R_S}} + u_g(t). & (48) \end{aligned}$$

With the updated quadrature, the new moments can be computed.

$$M_i^l(t+\Delta t) = \sum_{k=1}^{2} w_k(t) S_k(t+\Delta t)^l U_k(t+\Delta t)^i. \tag{49}$$

To account for more complex law, the strategy is slightly modified, the two differences lying on the flux determination and the ODE system that is needed to be solved. Considering $R_S(S)$ and $\mathrm{St}(S)$, the evaluation of the disappearance flux of droplets is now:

$$F_i^l = \int_0^{S_{lim}(t)} U(S)^i S^l n_l(S) \mathrm{d}S, \tag{50}$$

where S_{lim} is obtained by solving the non-linear system backward in time:

$$\begin{cases} \dfrac{\mathrm{d}S_{lim}}{\mathrm{d}t} = R_S(S_{lim}), \\ S_{lim}(t+\Delta t) = 0, \end{cases} \tag{51}$$

which means that S_{lim} is the biggest size that reaches the zero size during one timestep. Using this flux, the corrected moments are computed and the same quadrature is performed, as with simple laws. Then, the obtained system of ODE is solved:

$$\begin{cases} \dfrac{\mathrm{d}U_k}{\mathrm{d}t} = -\dfrac{1}{\mathrm{St}(S)}\left(U_k - u_g\right), \\ \dfrac{\mathrm{d}S_k}{\mathrm{d}t} = R_S(S), \end{cases} \tag{52}$$

by using an ODE solver. Solving this system of ODE allows to reach the updated moments in the same manner as with simple laws.

5.1.2. Evaluation in 0D test cases

0D test cases are used to evaluate the ability of the CSVM to account for both drag and evaporation. For all cases, the initial liquid velocity distribution is constant and set to 1. The initial size distribution is a normal distribution $n(S) = 1/(\sqrt{2\pi}\sigma)\exp(-(S-\mu)/2\sigma^2)$ with $\sigma = 0.4$ and $\mu = 0.6$. The Stokes number at $S = 1$ is set to 1. Then the test cases are defined by two parameters: the gas velocity as a function of time, $u_g(t)$, and the evaporation rate R_S.

The Lagrangian reference is computed using a tracking of 10^6 particles randomly chosen to fullfill the normal distribution $n(S)$. Eulerian quantities for the reference solution are obtained by projection of the Lagrangian particles over the Eulerian grid.

The combined effect of drag force and evaporation is evaluated. Evaporation is the first motivation of the EMSM, and its accuracy has already been demonstrated in [15]. The novelty of this work is the ability to achieve a good accuracy on size-velocity moments. Here we consider $R_S = 1$ and $u_g = 0.5\cos(10t)$.

The evolution of moments against time for Lagrangian, CSVM and EMSM are plotted in Fig. 8. For size moments, the results are the same for CSVM and EMSM, as the size reconstruction is still the same. For size-velocity moments, results are better for the CSVM. This result is confirmed by Fig. 9, on which the error for size and size-velocity moments is plotted. For the CSVM, the error is under 3% where it reaches 10% without velocity reconstruction, and this with only one additional moment.

To investigate the ability of the proposed method to capture a more complex dynamic, this test case will consider no evaporation ($R_S = 0$) and a variable gas velocity with three modes, plotted in Fig. 10:

$$u_g(t) = \frac{1}{2}\cos(4\pi t) \text{ if } t \leq 1, \tag{53}$$

$$= \cos(\pi t) \text{ if } 1 < t \leq 5, \tag{54}$$

$$= \frac{1}{4}\cos(8\pi t) \text{ if } t > 5. \tag{55}$$

These three modes are expected to mimic what can be seen by particles going through several vortices with different properties. In Fig. 11, the evolution of size-velocity moments against time for CSVM and EMSM. The improvement of the velocity reconstruction is obvious, the error on M_1^1 being undistinguished with velocity reconstruction. These results are confirmed again by the error in Fig. 12, which stays under 2% with reconstruction and reaches more than 10% without.

Finally, the CSVM is able to capture the phase space evolution due to evaporation and drag force of a dispersed phase, by using only one additional moment comparing to the EMSM, which cannot capture the evolution of size-velocity moments.

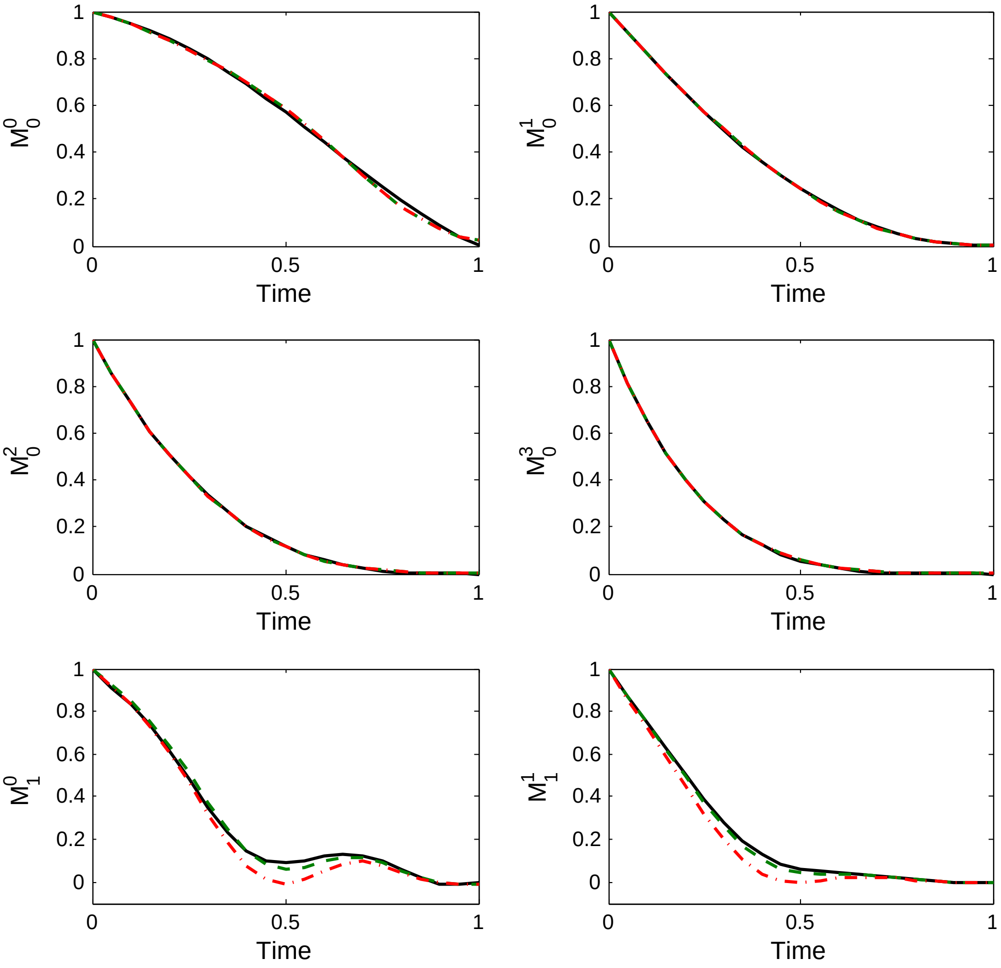

Figure 8: Evolution of resolved moments: Lagrangian reference (solid line), CSVM (dashed line), and EMSM (dot-dashed line).

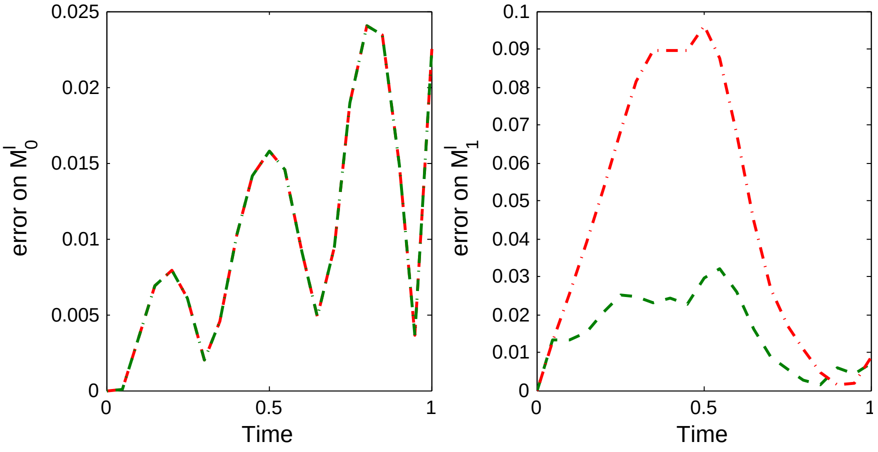

Figure 9: Evolution of the maximal error on size (left) and size-velocity moment (right) vectors comparing to the Lagrangian reference: CSVM (dashed line), and EMSM (dot-dashed line) for size moments (left) and size-velocity moments (right).

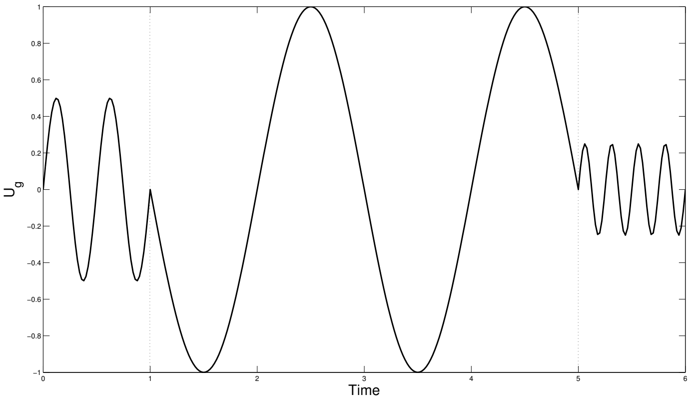

Figure 10: Evolution of the gas velocity against time.

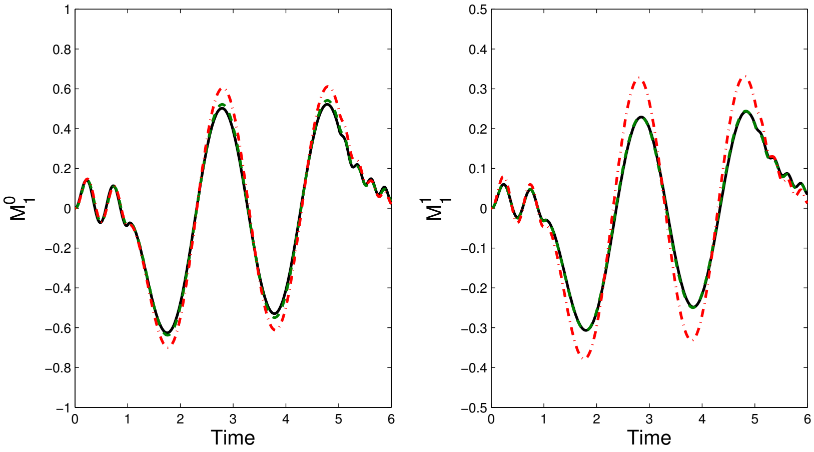

Figure 11: Evolution of resolved moments: Lagrangian reference (solid line), CSVM (dashed line), and EMSM (dot-dashed line).

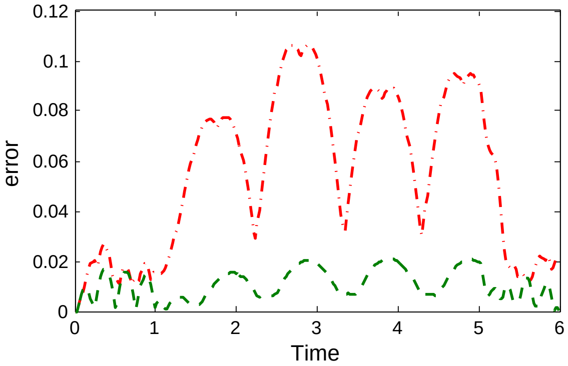

Figure 12: Evolution of the maximal error on size-velocity moments M_1^0 and M_1^1 comparing to the Lagrangian reference: CSVM (dashed line), and EMSM (dot-dashed line).

5.2. Convection scheme

The physical space evolution is surely the most important part of the size-velocity correlation. As seen in previous section, the constant velocity assumption, even if it leads to higher errors, does not lead to a completely different moment evolution in the velocity phase space. But in physical space, as shown by Fig. 1, the dynamics will be totally different. The moment equation for the transport in physical space in one dimension is:

$$\frac{\partial \mathcal{M}}{\partial t} + \frac{\partial \mathcal{F}(\mathcal{M})}{\partial x} = 0, \tag{56}$$

where $\mathcal{M} = (M_0^0, M_0^1, M_0^2, M_0^3, M_1^0, M_1^1)^T$ is the moment vector and $\mathcal{F}(\mathcal{M}) = (M_1^0, M_1^1, M_1^2, M_1^3, M_2^0, M_2^1)^T$ is the flux vector. For a constant velocity distribution, the fluxes are linear functions of the moments. In this case, a first order finite-volume scheme preserves the moment space, as it is positive definite and the scheme reconstruction generates realizable moments. The second-order scheme that preserves the moment space is much more difficult to design, and this issue raised in the literature [26] had been finally tackled in [20]. In the case of a continuous non-constant velocity, fluxes are now a complex function of the moments, and designing a specific scheme becomes necessary.

5.2.1. Flux splitting kinetic scheme

The moment equation is related to the following one dimensional kinetic equation:

$$\frac{\partial f}{\partial t} + v\frac{\partial f}{\partial x} = 0, \tag{57}$$

where $f(t, x, v, S) = n(t, x, S)\delta(v - U(t, x, S))$. Integrating over velocities but not over sizes, the following infinite system for $S = [0, 1]$ is found:

$$\begin{aligned} \frac{\partial n(S)}{\partial t} + \frac{\partial n(S)U(S)}{\partial x} &= 0, \\ \frac{\partial n(S)U(S)}{\partial t} + \frac{\partial n(S)U(S)^2}{\partial x} &= 0. \end{aligned} \tag{58}$$

To solve this system, a first order upwind finite volume scheme is used:

$$n_j^{n+1} = n_j^n - \frac{\Delta t}{\Delta x}\left(F_{j+1/2} - F_{j-1/2}\right), \tag{59}$$

$$n_j^{n+1}U_j^{n+1} = n_j^n U_j^n - \frac{\Delta t}{\Delta x}\left(G_{j+1/2} - G_{j-1/2}\right), \tag{60}$$

where:

$$F_{j+1/2} = \min(0, U_{j+1}^n)n_{j+1}^n + \max(0, U_j^n)n_j^n, \tag{61}$$

$$G_{j+1/2} = \min(0, U_{j+1}^n)n_{j+1}^n U_{j+1}^n + \max(0, U_j^n)n_j^n U_j^n. \tag{62}$$

By integrating over size, the following scheme is obtained:

$$\mathcal{M}_j^{n+1} = \mathcal{M}_j^n - \frac{\Delta t}{\Delta x}\left(\mathcal{F}_{j+1/2} - \mathcal{F}_{j-1/2}\right), \tag{63}$$

where the fluxes are splitted into positive and negative components:

$$\mathcal{F}_{j+1/2} = \int_0^1 \mathcal{S}\left(\min(0, U_{j+1}^n)n_{j+1}\mathcal{U}_{j+1}^n + \max(0, U_j^n)n_j\mathcal{U}_j^n\right) \mathrm{d}S = \mathcal{F}_{j+1}^- + \mathcal{F}_j^+, \tag{64}$$

where $\mathcal{S} = [1, S, S^2, S^3, 1, S]^T$ and $\mathcal{U}_j^n = [1, 1, 1, 1, U_j^n, U_j^n]^T$. Using the size and velocity reconstructions these fluxes can be computed for every moments using the adaptive integration method proposed for the EM. To ensure the stability of the scheme, a CFL condition is imposed on the timestep which is also based on the velocity reconstruction:

$$\Delta t < \mathrm{CFL}\frac{\Delta x}{\max_S(|U(S)|)}. \tag{65}$$

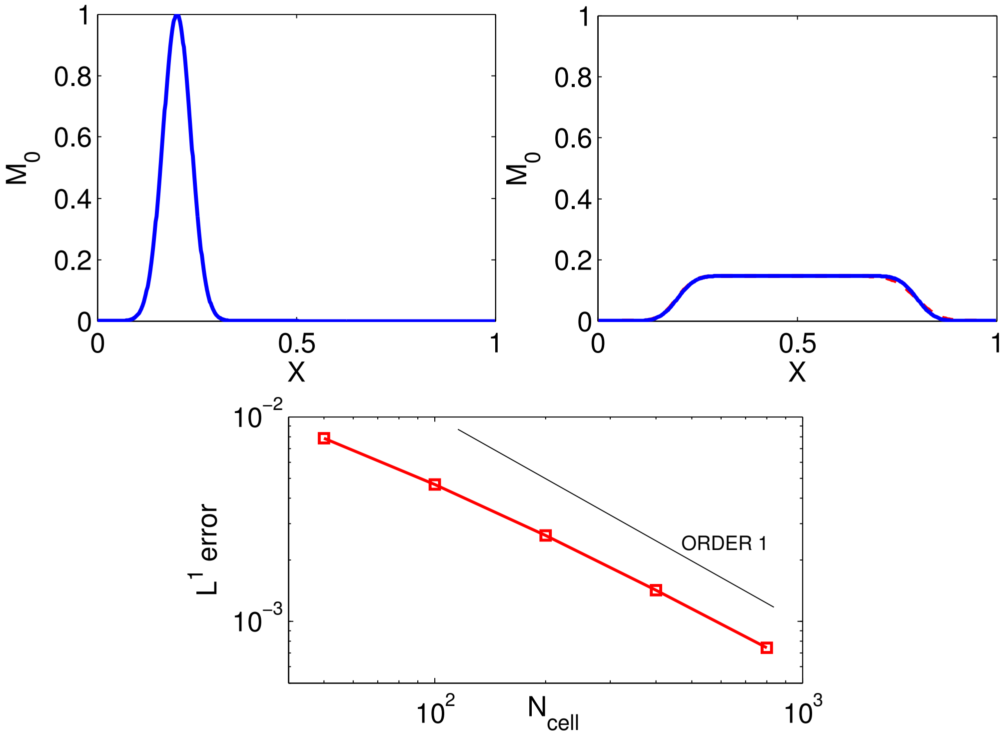

Figure 13: 1D test case: initial total droplet number distribution (upper left), analytical solution at $t = 0.6$ (upper right, full line), CSVM solution at $t = 0.6$ for 400 cells (upper right, dashed line), absolute error against cell number (down).

5.2.2. 1D case

The proposed scheme is evaluated on a 1D test case. The spatial distribution is gaussian, the NDF is constant in size, and the velocity is linear in size:

$$n(t=0,x,S) = \exp\left(-\frac{(x-x_c)^2}{\sigma^2}\right), \tag{66}$$

$$U(t=0,x,S) = U_g + (U_{max} - U_g)S. \tag{67}$$

Here $x_c = 0.2$, $\sigma = 0.05$, $U_g = 0$, $U_{max} = 1$. The analytical solution for M_0^0 at time $t = 0.6$ is:

$$M_0^0(x,t) = \frac{\sigma\sqrt{\pi}}{2t(U(S=1)-U_g)}\left[\operatorname{erf}\left(\frac{U(S=1)t + x_c - x}{\sigma}\right) - \operatorname{erf}\left(\frac{U_g t + x_c - x}{\sigma}\right)\right]. \tag{68}$$

Results are plotted in Fig. 13. The total droplet number is spread by the velocity distribution, and the agreement between analytical and CSVM solutions is satisfactory. The order of the scheme is close to 1, and the method converges to the analytical solution.

6. Application to more complex cases

Three 2D complex cases are investigated: the crossflow, the Taylor-Green vortices and the free jet. The first one consists in the injection of particles in the normal direction of a constant gas flow, which leads to a high size segregation and exhibits a steady solution. The second one consists in four contra-rotating vortices in a periodic domain. This case also leads to a high size segregation, but is more complicated as the gas velocity is not uniform and imposes that there is no steady solution here. Those two test cases are set to evaluate the proposed method to capture limiting case, i.e. where all moment sets in the domain tends to the frontier of the moment space. In practical applications, the NDF tends to smooth size distributions because of the turbulent mixing for example (see [27] where polydispersity is exactly generated from a monodisperse spray through evaporation and turbulent mixing). The last test case is closer to pratical applications. it consists in the injection of particles into a weakly turbulent free jet. As our analysis will be focused on the dynamics of a polydisperse cloud of droplets, these test cases are non-evaporating.

6.1. Crossflow

The crossflow generates monodisperse distributions due to drag force size-conditioned segregation. As monodisperse distributions are at the frontier of the moment space, it is an interesting case to confirm the ability of the EM to capture such distributions. Moreover considering that every size has its proper velocity and trajectory, it is also a good case for evaluating the transport scheme.

The size of the computational domain is 2 in x direction and 1 in y direction. The injection is made between $X_L = 0.1$ and $X_R = 0.3$, at a constant velocity $V_0 = 1$ and $U_0 = 0$, with a constant number distribution $n(t, x, S) = 1$. The gas flow is uniform with $U_g = 1$ and $V_g = 0$. The semi-analytical solution is described in Appendix 8.B.

In Fig. 14, the droplet number density is shown for the Multifluid approach with 10 and 40 sections, and the CSVM with 4 moments in size and 2 moments in size-velocity. The Multifluid approach considers only one Stokes number for each section, so each section will have only one dynamics, even if the section covers a wide spectrum of Stokes numbers. The effect of such a size discretization is strong with 10 sections (30 moments, 10 in size, 2×10 in velocity), with 10 distinct trajectories. This effect become less pronounced with 40 sections (120 moments). With the CSVM, as the whole spectrum of Stokes number in the distribution is considered, a continuous number density distribution is obtained. And this is done with only 8 moments[1].

In Fig. 15, Multifluid approach with 10 and 40 sections, CSVM and analytical solution for the number density distribution and mean surface against Y are compared at the right outlet of the domain. The highly oscillatory behaviour of the 10 sections Multifluid solution is exhibited. The 40 sections Multifluid solution is in good agreement with the analytical solution. The CSVM captures a continuous distribution, but exhibits a large scale oscillation. In fact the results are encouraging for a 8 moments solution (to be compared with the 30 and 120 moments for Multifluid solution). The quality of the dynamical structure of the solution is confirmed by the mean size. All the method captures relatively well the size distribution, with the worse results for the 10 sections Multifluid and better results for the 40 sections Multifluid. This test case also demonstrates the ability and the robustness of the CSVM to capture high segregation effects with a limited number of moments.

6.2. Taylor Green vortices

The Taylor Green vortices case is more complex than the Crossflow, as it is an unsteady configuration. The segregation effect is strong, small droplet being captured by the vortices, whereas big droplets can move from one to another. The computational domain is $[0, 1]^2$ and periodic in each direction. The gas velocity is:

$$U_g(X,Y) = \quad cos(2\pi X)sin(2\pi Y), \tag{69}$$

$$V_g(X,Y) = \; - \; sin(2\pi X)cos(2\pi Y). \tag{70}$$

Droplets with a Stokes number higher than the critical Stokes number $\mathrm{St}_c = 1/8\pi$ can exhibit trajectory crossings, and thus a monokinetic eulerian approach (one velocity per size in this work) can generate δ-shock as the system is weakly hyperbolic [28, 29]. The behaviour of our scheme in such a case is analysed in Appendix 8.A and demonstrates its robustness.

---

[1] Let us mention, that for the sake of the presentation of fair comparisons, we have used a first order version of the multi-fluid model (as well as EMSM in the following when it is used). However, whereas we still do not have a second order version of the present scheme, the Multifluid as well as the EMSM model admit a second order extension for the transport in physical space which allow less numerical diffusion.

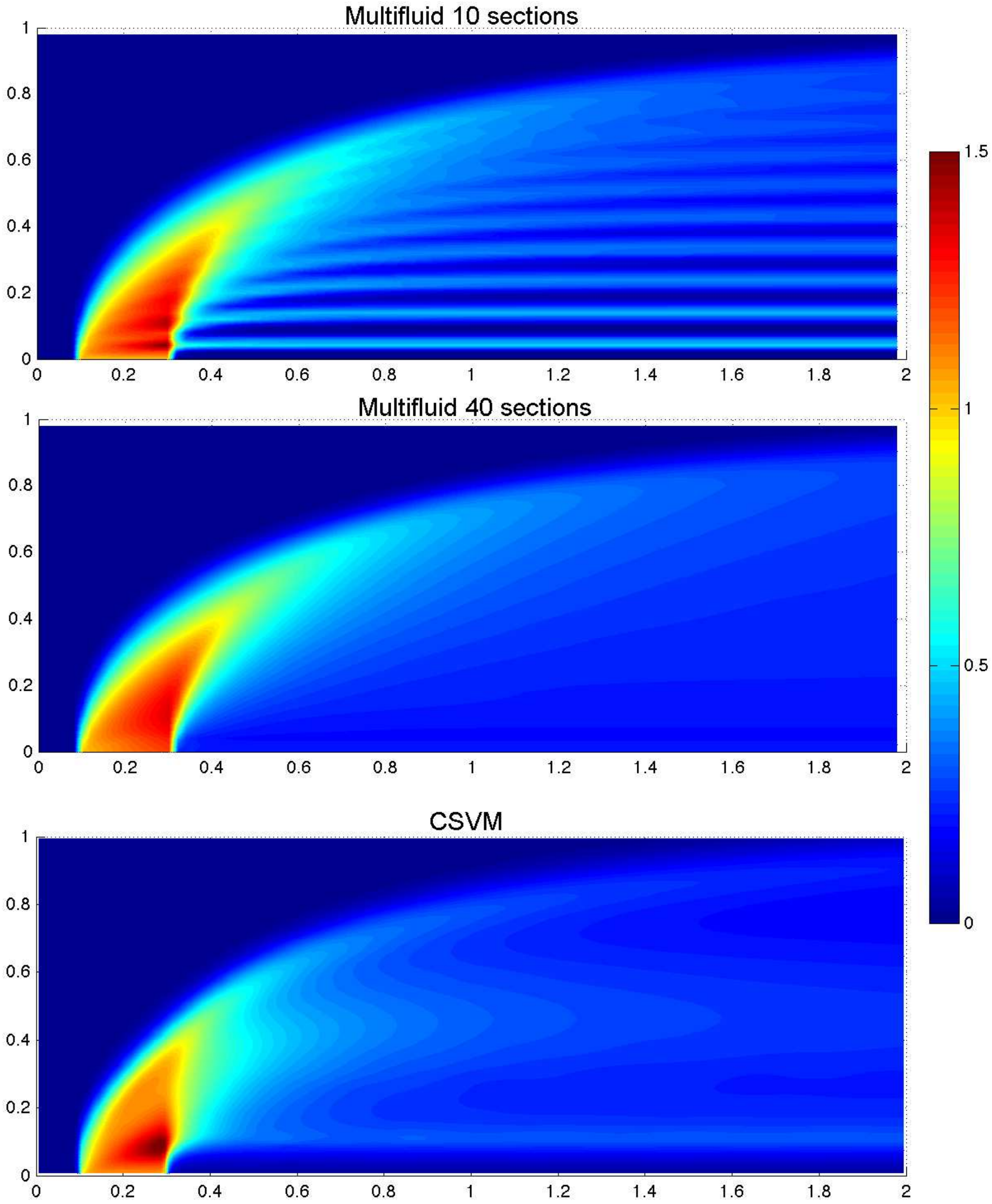

Figure 14: 2D Crossflow: droplet number density for the Multifluid approach with 10 sections (up) and 40 sections (center), and for the CSVM (down).

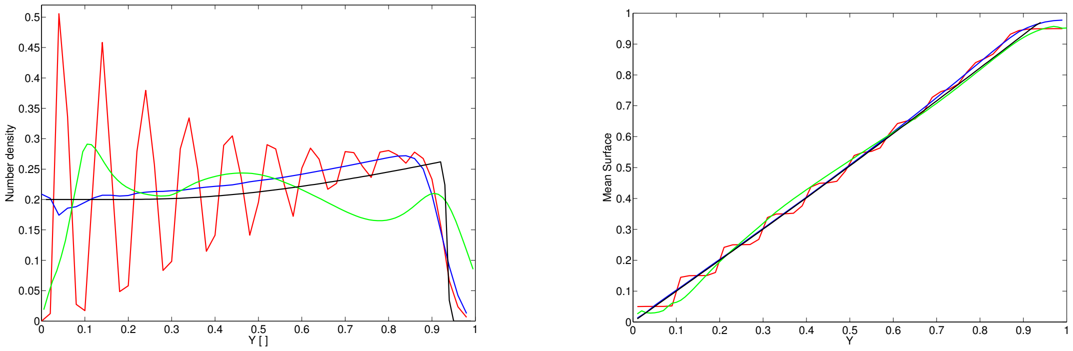

Figure 15: 2D Crossflow: droplet number density (left) and mean surface (right) at $X = 2$ against Y for the Multifluid approach with 10 sections (red line) and with 40 sections (blue line), the CSVM (green line) and the analytical solution (black line).

The initial number density distribution is :

$$
\begin{aligned}
n(x, y, t, S) &= \frac{\sin(\pi W R)}{\pi W R}, \qquad (71) \\
R &= \sqrt{(x - x_c)^2 + (y - y_c)^2}, \qquad (72)
\end{aligned}
$$

where $W = \sqrt{10}$ and $[x_c, y_c] = [0.275, 0.825]$. The size interval is $[0, 20\mathrm{St}_c]$ where $\mathrm{St}_c = 1/8\pi$. The initial droplet velocity is equal to the gas velocity. Since no analytical solution can easily be obtained, a Lagrangian reference solution is proposed, the solver being described in Appendix 8.C.

In Fig. 16, the droplet number density and the mean surface for one section Multifluid, 40 sections Multifluid, Lagrangian, and CSVM are shown at time $t = 1$. The one section Multifluid solution shows the effect of having one velocity for the whole size distribution. Comparisons of the Lagrangian reference solution, the 40 sections Multifluid and the CSVM show a really good agreement. For the mean surface, the results of the CSVM are in really good agreement compared to the Lagrangian reference, and confirm the great accuracy of the method to capture the size-conditionned dynamics.

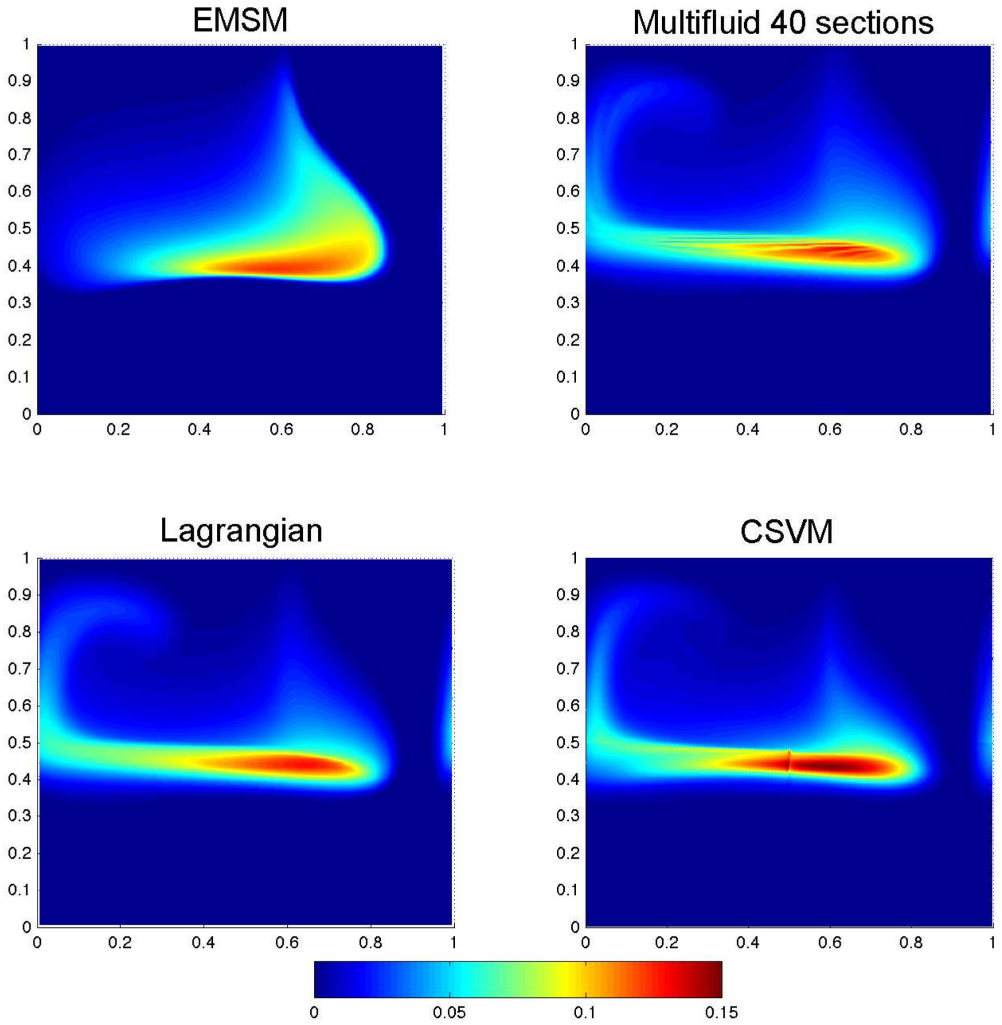

Figure 16: Taylor-Green vortices: droplet number density for the EMSM approach (upper left) and with 40 sections (upper right), the Lagrangian tracking with 10^8 particles, and the CSVM.

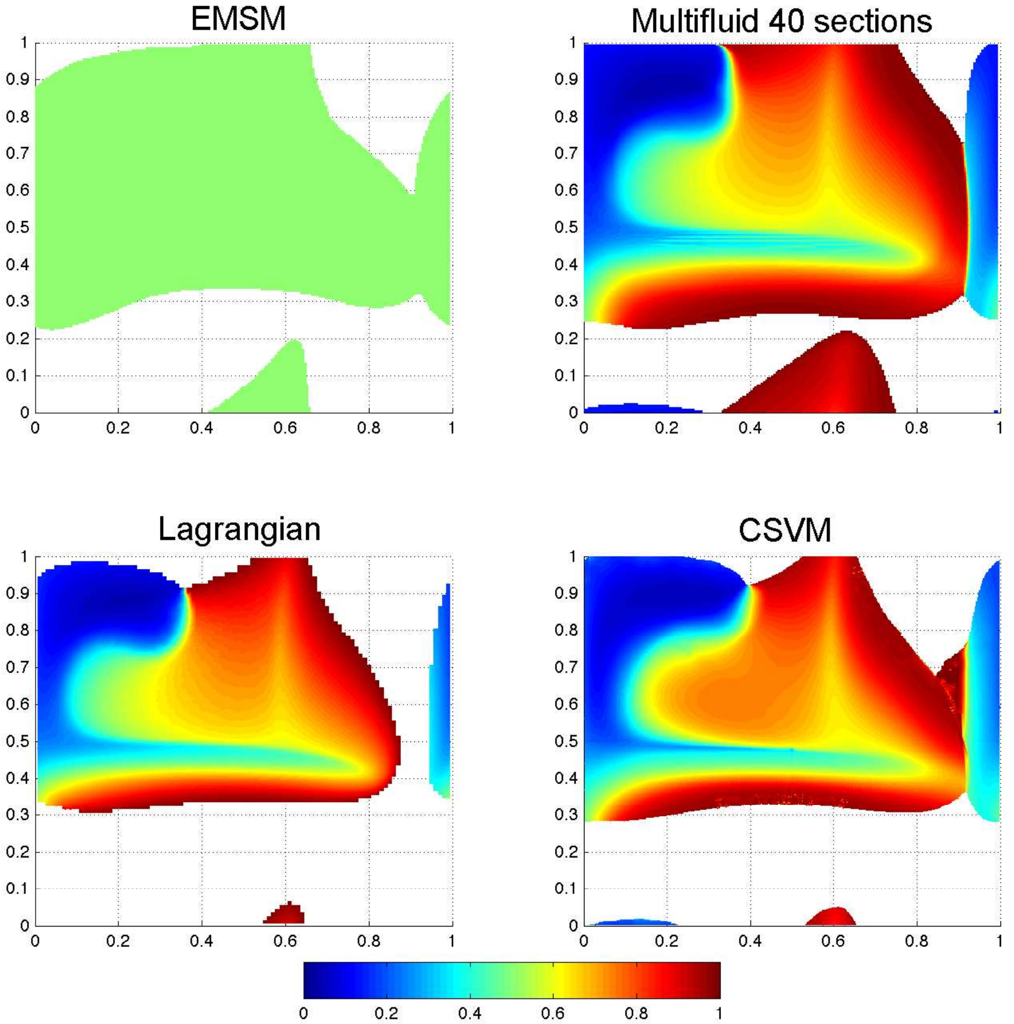

Figure 17: Taylor-Green vortices: mean surface for the EMSM approach (upper left) and with 40 sections (upper right), the Lagrangian tracking with 10^8 particles, and the CSVM.

6.3. *Weakly turbulent Free jet*

In this last test case, we consider an unsteady weakly turbulent free jet originally introduced in the Ph.D. Thesis of Hicham Meftah at CORIA [30]. It is generated using the ASPHODELE solver, developed at CORIA by Julien Reveillon and collaborators [31, 32], which uses a low Mach solver for the gas phase. Kah et al. [20] show the ability of the EMSM to reproduce this case in evaporating conditions, but for a range of low Stokes numbers where differential size-conditioned dynamics have a limited impact on the global spray dynamics. In the present case, in order to assess the accuracy and potential of the method, we rather study a non-evaporating case with a much larger range of Stokes number where size-conditioned differential dynamics result are important.

The free jet Reynolds number based on U_0, ν_0 and L_0 is 1000. For illustration purpose, dimensional quantities are given, the solver using non-dimensional quantities. $U_0 = 1$ m/s is the injection velocity, $\nu_0 = 1.5 \times 10^{-3}$ m^2/s the gas viscosity, and $L_0 = 1.5$ cm the jet width. To destabilize the jet, turbulence is injected using the Klein method with 10% fluctuations so that $U_0' = 0.1$ m/s [33]. The vorticity field is presented in Fig. 18. The Stokes number relative to the gas fluctuations time scale $\tau_g = L_0/U_0'$ of the injected particles ranges from St = 0 to St = 6.66.

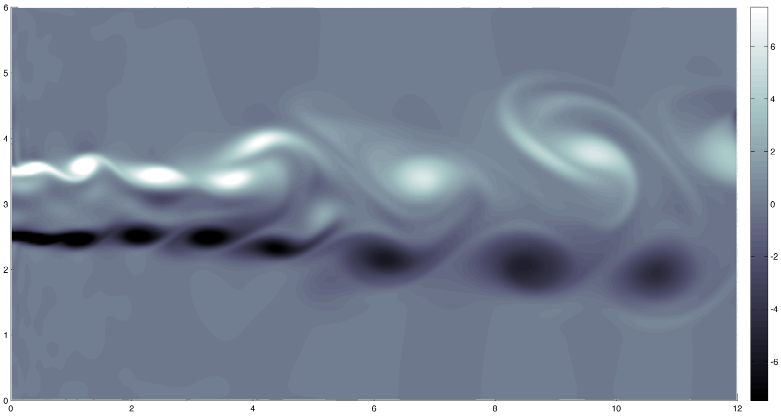

Figure 18: Free jet: vorticity field for the gas phase at time $t = 20$ s.

Figure 19 and Fig. 20 show the number density and the mean surface for the EMSM and ten section Multifluid approaches, the Lagrangian method and the CSVM. All methods capture relatively well the number density repartition, even if the one section EMSM cannot captures the dynamics of small droplets which are staying longer inside the vortices.

In Figs. 21-22, the number density for small droplets ($S = [0.0, 0.1]$) and big droplets ($S = [0.9, 1.0]$) are shown. Now, where the EMSM captures the same repartition for small and big droplets, the Multifluid approach and the CSVM are able to reproduce the differential dynamics for each size intervals: the big droplets are ejected from the large vortices of the free jet, whereas small droplets stay into them.

Those results are confirmed by the mean surface plotted in Fig. 20. The Lagrangian result shows the high size segregation induced by the vortices. The ten sections Multifluid approach and the CSVM reproduce really accurately this segregation, even if the numerical diffusion due to the first order convection schemes tends to diffuse the thin structures appearing in the Lagrangian simulation[2].

In thus becomes clear that the CSVM method provides an accurate high order moment method, which is able to capture the size conditioned dynamics of a polydisperse spray with a large range of Stokes number,

---

[2] Once again, for the sake of fair comparisons, we have used a first order scheme for all Eulerian simulations.

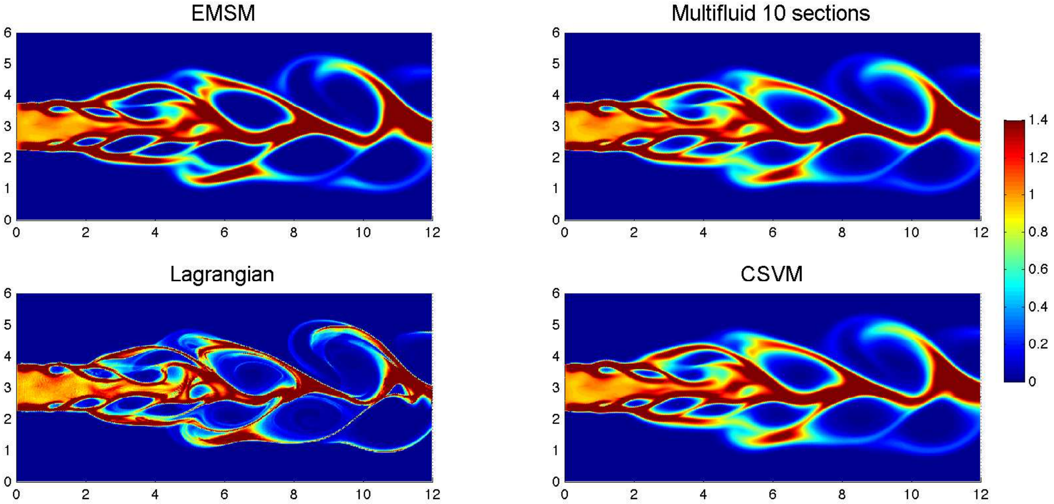

Figure 19: Free jet: droplet number density for the EMSM approach with one section (upper left) and with Multifluid 10 sections (upper right), the Lagrangian tracking with 10^8 particles, and the CSVM.

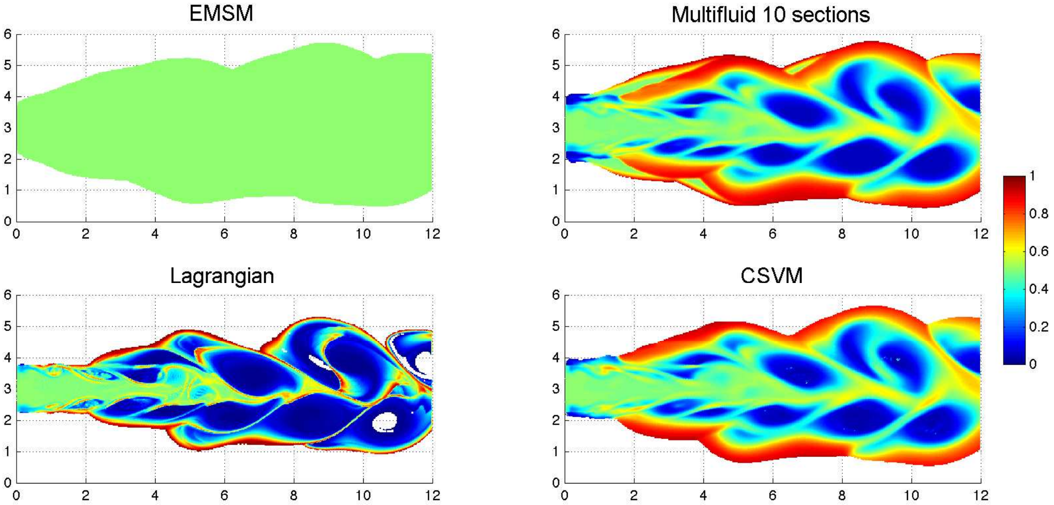

Figure 20: Free jet: mean surface for the EMSM approach with one section (upper left) and with Multifluid 10 sections (upper right), the Lagrangian tracking with 10^8 particles, and the CSVM.

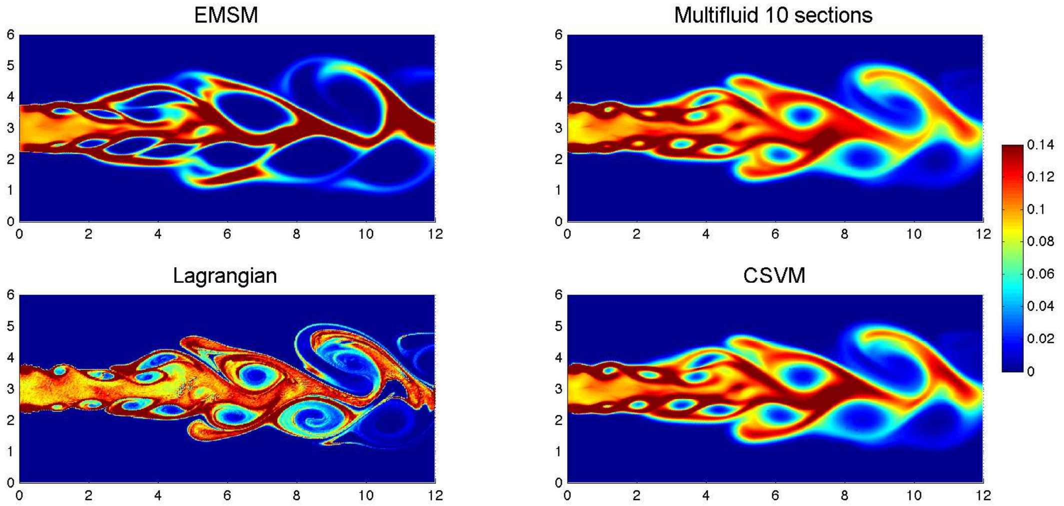

Figure 21: Free jet: droplet number density in $S = [0.0, 0.1]$ for the EMSM approach with one section (upper left) and with Multifluid 10 sections (upper right), the Lagrangian tracking with 10^8 particles, and the CSVM.

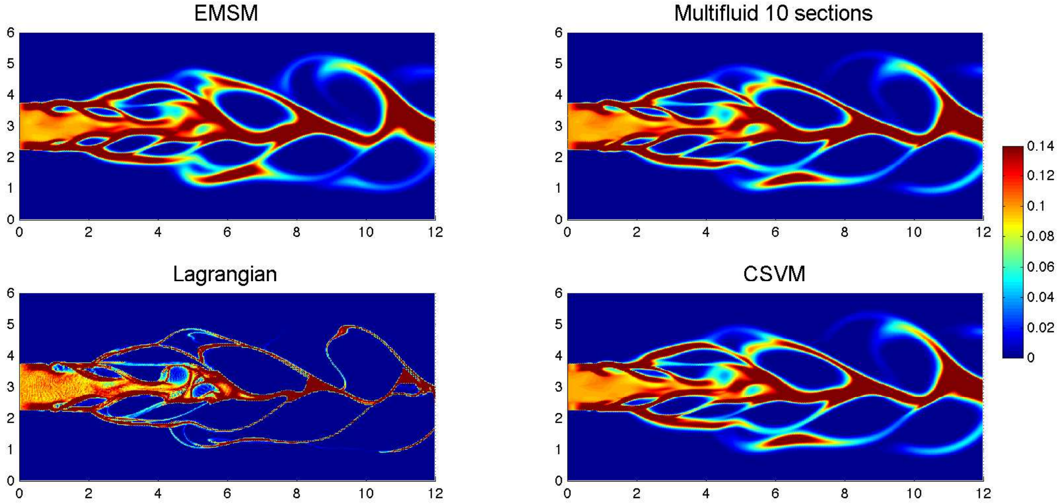

Figure 22: Free jet: droplet number density in $S = [0.9, 1.0]$ for the EMSM approach with one section (upper left) and with Multifluid 10 sections (upper right), the Lagrangian tracking with 10^8 particles, and the CSVM.

successfully coping with the singularities at the frontier of the moment space where the dynamics tend to converge due to the size-segregation capabilities of the chosen gaseous flow fields.

In the proposed laminar configurations we have chosen, the potential of the method has been highlighted and will lead to large memory storage savings in the case of 3D cases. In terms of computational cost, even if the configurations chosen in the present study are not favorable (since for example there is no subgrid turbulent mixing which will take the moment vector further from the frontier of the moment space), the CSVM method leads to a computational cost of the same order as the Multifluid with 24 sections. Actually, the two important building block of the CSVM are the reconstruction strategy and the convection scheme. For 1000 iterations, 185 s are spent for the reconstruction step, whereas 492 s are spent for the convection scheme out of a total of 811 s. As these two steps are essentially made of integral evaluations, it seems clear that the last issue that we will have to tackle now is the efficiency of the evaluation of such integrals, even if our method demonstrates its ability to reproduce the full physics of such polydisperse flows and is very promising as an extension of EMSM for industrial LES applications [23, 22].

7. Conclusions and outcomes

In this paper, the high order moment method CSVM has been introduced in order to capture both polydispersion as well as to account for size-velocity correlations, based on the EMSM of [20]. Basically, whereas the initial EMSM considered only one velocity for all sizes, which is efficient for a range of small Stokes numbers, a broader spectrum of Stokes numbers can lead to very diverse size-conditioned dynamics and the necessity to be able to model such a phenomenon has become clear. We have also seen that size-conditioned dynamics can lead to particle size segregation and moment vectors very close to the frontier of the moment space, where the EM method usually experiences difficulties.

First, the entropy maximization has been improved, in order to be able to reproduce size distributions close to the frontier of the moment space. Actually, the initial algorithm proposed in [15] is able to build NDF with canonical moments in $[0.01, 0.99]$. To cover a larger part of the moment space, a Gauss-Legendre method with an adaptive support has been implemented, in such a way that quadrature points are used only where droplets lies. Furthermore, the Newton solver has been optimized by adapting the number of parameters of the EM and by tabulating the initial guess. Size-velocity correlations have been accounted for, by using one additional moment in size-velocity for each direction. Using a power reconstruction and an equilibrium constraint for droplets of zero size allow to reconstruct the velocity for each size. The evolution in phase space by drag force and evaporation has been performed by evaluating the disappearance flux at zero size and the shift in size using a quadrature method similar to CQMOM. We emphasize the fact that combining EMSM with a quadrature approach for the phase space evolution allows to use arbitrary evaporation and drag laws.

The evolution in physical space has been done by using a flux splitting kinetic scheme, which separates positive and negative components of the fluxes to obtain an upwind scheme. By integrating this scheme over size, a realizable scheme is obtained, which is able to reproduce the proper dynamics of each size. This method has proven to be efficient in 1D cases.

Finally, the CSVM method has been applied on three complex cases: the crossflow, the Taylor-Green vortices and the weakly turbulent free jet. Both cases are very properly reproduced by the CSVM with only 8 moments, whereas the Multifluid approach need at least ten sections and 30 moments to be efficient.

In future work, three issues still need to be investigated. The convection scheme need to be improved to reach high order, and reduce the numerical diffusion of such a first order scheme. The proposed formalism will be extended to the framework of turbulent dynamics and subgrid scale models, to be able to capture size-conditionned velocity dispersion induced by the large scales of turbulence. Finally, we need to improve and optimize the integral evaluation algorithms for both reconstruction and transport in real space and compare such an approach in more realistic configurations with turbulent mixing, as the highly segregative cases of the present work impose to reconstruct NDF at the frontier of the moment space almost everywhere in the domain, increasing the computational cost due to the high number of iterations of the EM algorithm.

Acknowledgments

We would like to thanks Damien Kah for several helpful discussions and for providing numerous inputs and code sources from his Ph.D. Thesis where the EMSM was introduced. The motivation for the present study also stems from an original study of the crossflow configuration conducted in the Ph.D. Thesis of A. Vié as well as from discussions with his advisers S. Jay (IFPEN) and B. Cuenot (CERFACS), whom we take the occasion to thank here. The support from the RTRA DIGITEO as well as from Ecole Centrale Paris through the "Direction de la Recherche" for the Post-doctoral fellowship for A. Vié is gratefully acknowledged. In fact the present study received a funding from this RTRA through the MUSE project (PI M. Massot - "MUltiscale Spray combustion fully Eulerian solver in 3D : a new generation of numerical methods and algorithms, high performance simulations, validation and visualization"). We also acknowledge the computational resources of the Mesocentre of Ecole Centrale Paris where some of the simulations were performed.

8. Appendix

8.A. Ability to capture Delta-Shock

Even if the proposed extension of the CSVM is able to capture the velocity associated with each size, it cannot capture the trajectory crossing for each size. Because the underlying semi-kinetic system is weakly hyperbolic, this will generate δ-shock. To evaluate the ability of the proposed method to capture accurately δ-shock for each size, a 1D test case which is motivated by the Taylor-Green vortices is investigated. This configuration was further analysed in [28, 29].

In a 1D domain $[-\pi, \pi]$, a steady gas velocity field is set with $u_g = -\sin(x)$. Droplets are distributed uniformely at $t = 0$ with a null velocity and a constant droplet number density in size in the interval $[0, 20\mathrm{St}_c]$ where $\mathrm{St}_c = 1/8\pi$. In this test case all trajectories meet at $x = 0$, generating a central δ-shock, which is fed by all sizes progressively.

In Fig. 23, droplet number density is plotted at different times. It confirms the ability of the scheme to capture δ-shock accurately. In Fig. 24, the comparison of the Multifluid with 1000 sections and the CSVM confirms the ability of the method to capture size-conditionned dynamics, even in the case of δ-shock.

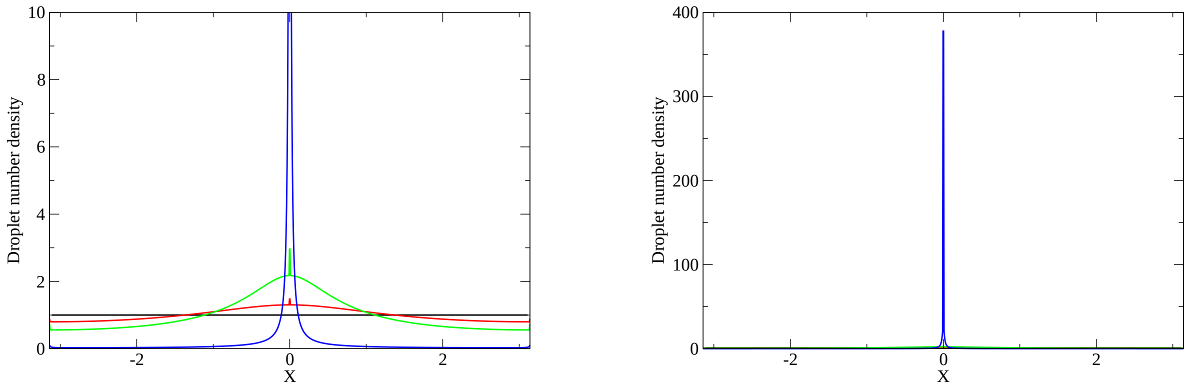

Figure 23: δ-shock generation: droplet number density zoomed on the initial solution (left) and at full scale (right) at time $t = 0$ (black line), $t = 0.5$ (red line), $t = 1.0$ (green line) and $t = 5.0$ (blue line)

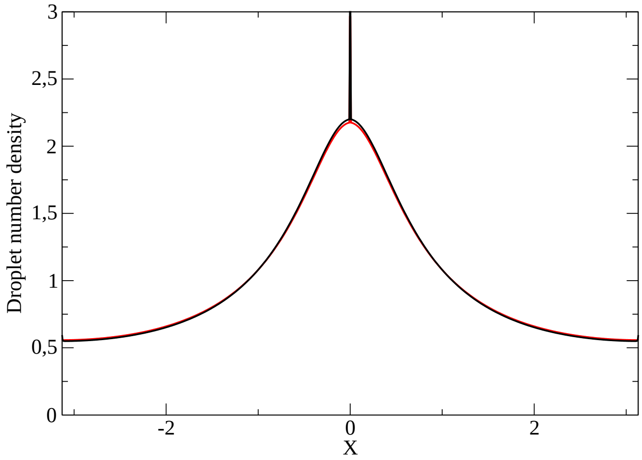

Figure 24: δ-shock generation: droplet number density at time $t = 1.0$ for CSVM (red line) and Multifluid with 1000 sections.

8.B. Analytic solution for the 2D Crossflow

An analytical solution is proposed for the stationary 2D crossflow configuration, based on the Lagrangian solution for each size, since no droplet crossing occurs for one size so that the Lagrangian and eulerian approaches are equivalent.

The Eulerian problem (2) with the monokinetic assumption $f(t, \mathbf{x}, \mathbf{v}, S) = n(t, \mathbf{x}, S)\delta(\mathbf{v} - \mathbf{u}(t, \mathbf{x}, S))$ and without evaporation is written as follow:

$$\begin{aligned} &\partial_t n + \partial_{\mathbf{x}}.(n\mathbf{u}) = 0, \\ &\partial_t(n\mathbf{u}) + \partial_{\mathbf{x}}.(n\mathbf{u} \otimes \mathbf{u}) = \frac{\mathbf{u_g} - \mathbf{u}}{K_d S}, \end{aligned} \tag{73}$$

with $\mathbf{u} = (U, V)$ the droplet velocity conditioned by size and $\mathbf{v_g} = (U_g, 0)$ the constant gas velocity. The steady state problem is considered on the domain $\mathbf{x} = (X, Y) \in [0, +\infty[\times[0, +\infty[$ with the following conditions on boundary $Y = 0$:

$$n(X, 0, S) = n^0 \mathbb{1}_{[X_L, X_R]}(X), \qquad U(X, 0, S) = 0, \qquad V(X, 0, S) = V^0, \tag{74}$$

with n^0 and V^0 some constants and with $n(X = 0, Y, S) = 0$ on the other incoming boundary.

Considering Lagrangian formulation, let (X_p, Y_p) and (U_p, V_p) be the position and the velocity of a droplet of size S. Its position at injection is $(X_p^0, 0)$, with $X_L < X_p^0 < X_R$ and its velocity is $(0, V^0)$. The evolutions of the droplet characteristics is given by:

$$\frac{dX_p}{dt} = U_p, \qquad \frac{dY_p}{dt} = V_p, \qquad \frac{dU_p}{dt} = \frac{U_g - U_p}{K_d S}, \qquad \frac{dV_p}{dt} = -\frac{V_p}{K_d S}. \tag{75}$$

So, the characteristics of droplets injected at time $t = t_0$ are:

$$\begin{aligned} &U_p(t) = U_g \left[1 - \exp\left(-\frac{t - t_0}{K_d S}\right)\right], && X_p(t) = X_p^0 + U_g \left\{t - t_0 + K_d S \left[\exp\left(-\frac{t - t_0}{K_d S}\right) - 1\right]\right\}, \\ &V_p(t) = V^0 \exp\left(-\frac{t - t_0}{K_d S}\right), && Y_p(t) = V^0 K_d S \left[1 - \exp\left(-\frac{t - t_0}{K_d S}\right)\right]. \end{aligned} \tag{76}$$

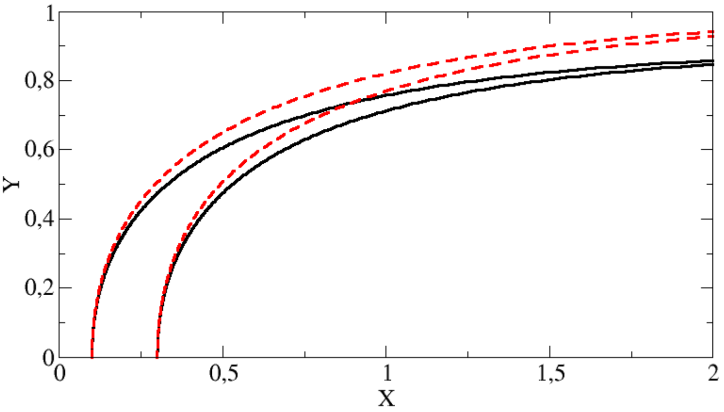

Figure 25: Position of droplets of size $S = 0.9$ (between solid lines) and $S = 1$ (between dashed lines).

Eliminating the variable t, the trajectories of such droplets are then characterized by the equation:

$$\frac{X_p - X_p^0}{U_g K_d S} = g\left(\frac{Y_p}{V^0 K_d S}\right), \tag{77}$$

where g is the increasing function from $[0, 1[$ to $[0, +\infty[$ defined by $g(y) = -\ln(1-y) - y$. Since droplets are injected between abscissa X_L and X_R, all droplets of size S are located in $[X_{min}(Y,S), X_{max}(Y,S)]$, with

$$X_{min}(Y,S) = X_L + U_g K_d S\, g\left(\frac{Y}{V^0 K_d S}\right), \qquad X_{max}(Y,S) = X_R + U_g K_d S\, g\left(\frac{Y}{V^0 K_d S}\right). \tag{78}$$

The position of such droplets is plotted on Fig. 25 for two sizes. This also implies that the droplets which can reach a given position (X,Y) with $X > X_R$ have a size S such that :

$$\frac{V^0}{U_g}(X - X_R) \leq h_Y(V^0 K_d S) \leq \frac{V^0}{U_g}(X - X_L), \tag{79}$$

where h_Y is the decreasing function from $]Y, +\infty[$ to $\mathbb{R}$ defined by $h_Y(x) = x\, g(Y/x)$. The size S of droplets reaching (X,Y) lives then in the interval $[S_{min}(X,Y), S_{max}(X,Y)]$, with

$$S_{min}(X,Y) = \frac{1}{V^0 K_d} h_Y^{-1}\left(\frac{V^0}{U_g}(X - X_L)\right), \qquad S_{max}(X,Y) = \frac{1}{V^0 K_d} h_Y^{-1}\left(\frac{V^0}{U_g}(X - X_R)\right). \tag{80}$$

Let us return to the Eulerian approach given by system (73). The droplet velocity (U,V) is given, thanks to the equivalence with the Lagrangian approach and thanks to equations (76), by

$$U(X,Y,S) = \frac{U_g Y}{V^0 K_d S}, \qquad V(X,Y,S) = V^0\left(1 - \frac{Y}{V^0 K_d S}\right), \qquad Y \in [0, V^0 K_d S[. \tag{81}$$

This velocity does not depend on X. Moreover, the injection is uniform in the interval $[X_L, X_R]$ and the number density is independent of X for $X \in [X_{min}(Y,S), X_{max}(Y,S)]$. The number density conservation for the size S is then given by $\partial(nV)/\partial Y = 0$ for $X \in [X_{min}(Y,S), X_{max}(Y,S)]$. Integrated between 0 and Y, it then induces:

$$n(X,Y,S) = \frac{V_0 n^0}{V(Y,S)} = \frac{n^0}{1 - \frac{Y}{V^0 K_d S}}, \qquad Y \in [0, V^0 K_d S[, \quad X \in [X_{min}(Y,S), X_{max}(Y,S)]. \tag{82}$$

Equations (81) and (82) give the analytical size conditioned velocity and the NDF, solution of (73). The total number density at (X,Y) plotted on Fig. 15 is then given by

$$\begin{aligned} n^{tot}(X,Y) &= \int_{S_{min(X,Y)}}^{S_{max}(X,Y)} n(X,Y,S)\mathrm{d}S \\ &= n^0 \left[\frac{Y}{V^0 K_d} \ln\left(\frac{V^0 K_d S_{max}(X,Y) - Y}{V^0 K_d S_{min}(X,Y) - Y} \right) + S_{max}(X,Y) - S_{min}(X,Y) \right] \end{aligned} \tag{83}$$

and the mean surface is

$$\begin{aligned} S_{mean}(X,Y) &= \frac{1}{n^{tot}(X,Y)} \int_{S_{min(X,Y)}}^{S_{max}(X,Y)} S\, n(X,Y,S)\mathrm{d}S \\ &= \frac{Y}{V^0 K_d} + \frac{n^0 \left(S_{max}(X,Y)^2 - S_{min}(X,Y)^2 \right)}{2\, n^{tot}(X,Y)}. \end{aligned} \tag{84}$$

8.C. Lagrangian solution for Taylor-Green vortices

The reference solution for the Taylor-Green vortices is chosen to be a Lagrangian computation, considering there is no analytical solution. This Lagrangian computation consists in a discrete particle simulation with a sufficiently high number of particles to achieve converged statistics. Considering that the gas velocity (U_g, V_g) is constant and given by

$$U_g(x,y) = \cos(2\pi x)\sin(2\pi y), \qquad V_g(x,y) = -\sin(2\pi x)\cos(2\pi y), \tag{85}$$

the problem to solve for each numerical particle is then written:

$$\frac{dX_p}{dt} = U_p, \qquad \frac{dY_p}{dt} = V_p, \qquad \frac{dU_p}{dt} = \frac{U_g(X_p,Y_p) - U_p}{K_d S}, \qquad \frac{dV_p}{dt} = \frac{V_g(X_p,Y_p) - V_p}{K_d S}, \tag{86}$$

for $p = 1, N_p$ where N_p is the number of particles. First, the initial conditions for each particles has to be given in such a way that the initial number density distribution is well reproduced. Second, a numerical scheme has to be given for the system (86).

The initial number density distribution is given by a cardinal sinus in physical space $[0,1]^2$ and a constant distribution in size space $[0,1]$:

$$n(x,y,S) = \frac{\sin\left(\pi W \sqrt{(x-x_c)^2 + (y-y_c)^2}\right)}{\pi W \sqrt{(x-x_c)^2 + (y-y_c)^2}} \qquad \text{if} \quad W\sqrt{(x-x_c)^2 + (y-y_c)^2} \le 1 \tag{87}$$

$$= 0 \qquad \text{if} \quad W\sqrt{(x-x_c)^2 + (y-y_c)^2} > 1 \tag{88}$$

so that $[x_c, y_c]$ is the center of the spatial distribution of the spray and W its width. To simplify, let consider cylindrical coordinates (r,θ) around the point $[x_c, y_c]$. The initial distribution is then, as a function of these new variables: $\tilde{n}(r,\theta,S) = r\frac{\sin(\pi\, W\, r)}{\pi\, W\, r}\mathbb{1}_{[0,1/W]}(r)\mathbb{1}_{[0,2\pi]}(\theta)\mathbb{1}_{[0,1]}(S)$. The rejection method is used to set numerical parcel with such distribution. Since $\tilde{n}(r,\theta,S)$ is smaller that $\mathbb{1}_{[0,1/W]}(r)\mathbb{1}_{[0,2\pi]}(\theta)\mathbb{1}_{[0,1]}(S)/(\pi W)$ this method leads to the following algorithm:

1. a uniform random number generator (here the native one of fortran) is used to generate uniform random variables $r \in [0, 1/W]$, $\theta \in [0, 2\pi]$, $S \in [0,1]$ and $T \in [0,1]$

2. if $\tilde{n}(r,\theta,S) > T/(\pi W)$ then the generated particle is conserved
3. otherwise the generated particle is rejected.

This algorithm is reproduced until the required number of particles is reached.

Once initial conditions are set for each particles, the Lagrangian system of equation (86) is solved in a semi-implicit manner. During one time step, the gas velocity is approximated by a constant. With this assumption, one can derive an analytical solution for position and velocity:

$$
\begin{aligned}
U_p(t+\Delta t) &= [U_p(t) - U_g(X_p(t),Y_p(t))]\exp\left(-\frac{\Delta t}{K_dS_p}\right) + U_g(X_p(t),Y_p(t)) \\
V_p(t+\Delta t) &= [V_p(t) - V_g(X_p(t),Y_p(t))]\exp\left(-\frac{\Delta t}{K_dS_p}\right) + V_g(X_p(t),Y_p(t)) \\
X_p(t+\Delta t) &= X_p(t) + U_g(X_p(t),Y_p(t))\Delta t + K_dS_p[U_p(t) - U_g(X_p(t),Y_p(t))]\left(1-\exp\left(-\frac{\Delta t}{K_dS_p}\right)\right) \\
Y_p(t+\Delta t) &= Y_p(t) + V_g(X_p(t),Y_p(t))\Delta t + K_dS_p[V_p(t) - V_g(X_p(t),Y_p(t))]\left(1-\exp\left(-\frac{\Delta t}{K_dS_p}\right)\right)
\end{aligned}
$$

In this approach, the only source of error is the variation of the gas velocity along the particle trajectory. This can give the intuition that this method is convergent with at least a first order accuracy. More rigorously, the convergence of the scheme is proven in what follow.

Let us denote $(U_p^e, V_p^e, X_p^e, Y_p^e)$ the exact solution of (86). For example, starting from a time t, the velocity in the first direction $U_p^e(t+\theta)$ is given by

$$
U_p^e(t+\theta) = U_p^e(t)\exp\left(-\frac{\theta}{K_dS_p}\right) + \int_0^\theta \frac{U_g(X_p^e(t+\tau),Y_p^e(t+\tau))}{K_dS}\exp\left(\frac{\tau-\theta}{K_dS_p}\right)d\tau \qquad (89)
$$

The same kind of formula can be written for the approximate solution $U_p(t+\theta)$, with no variation of the gas velocity:

$$
U_p(t+\theta) = U_p(t)\exp\left(-\frac{\theta}{K_dS_p}\right) + \int_0^\theta \frac{U_g(X_p(t),Y_p(t))}{K_dS}\exp\left(\frac{\tau-\theta}{K_dS_p}\right)d\tau \qquad (90)
$$

Moreover, the exact and approximated first coordinate is given by

$$
X_p^e(t+\tau) - X_p^e(t) = \int_0^\tau U_p^e(t+\theta)d\theta, \qquad X_p(t+\tau) - X_p(t) = \int_0^\tau U_p(t+\theta)d\theta, \qquad (91)
$$

Same kind of formula can be written for the second direction. So the absolute error on the velocity in the first direction is such that, for $\theta > 0$

$$
\begin{aligned}
|U_p^e(t+\theta) - U_p(t+\theta)| \;\; \leq \;\; & \left|U_p^e(t) - U_p(t)\right| \\
& + \frac{1}{K_dS}\int_0^\theta \left|U_g(X_p^e(t+\tau),Y_p^e(t+\tau)) - U_g(X_p(t),Y_p(t))\right|\exp\left(\frac{\tau-\theta}{K_dS_p}\right)d\tau.
\end{aligned}
$$

Since the spatial gradient of the gas velocity is smaller than 2π in both directions, and since both components of the particle velocity are smaller than one (the maximum of both components of the gas velocity), one can write

$$
\begin{aligned}
\left|U_g(X_p^e(t+\tau),Y_p^e(t+\tau)) - U_g(X_p(t),Y_p(t))\right| \;\; &\leq \;\; 2\pi\left(|X_p^e(t+\tau) - X_p(t)| + |Y_p^e(t+\tau) - Y_p(t)|\right), \\
&\leq \;\; 2\pi\left(2\tau + |X_p^e(t) - X_p(t)| + |Y_p^e(t) - Y_p(t)|\right),
\end{aligned}
$$

so that, when $\theta/(K_dS)$ tends to zero

$$
|U_p^e(t+\theta) - U_p(t+\theta)| \leq \left|U_p^e(t) - U_p(t)\right| + 2\pi\left(|X_p^e(t) - X_p(t)| + |Y_p^e(t) - Y_p(t)|\right) + \theta\, O\left(\frac{\theta}{K_dS}\right) \qquad (92)
$$

and, thanks to (91)

$$\begin{aligned}
|X_p^e(t+\Delta t) - X_p(t+\Delta t)| &\leq |X_p^e(t) - X_p(t)| + \int_0^{\Delta t} |U_p^e(t+\theta) - U_p(t+\theta)| d\theta \qquad (93) \\
&\leq (1 + 2\pi\Delta t)\,|X_p^e(t) - X_p(t)| + \Delta t \left|U_p^e(t) - U_p(t)\right| + 2\pi\Delta t |Y_p^e(t) - Y_p(t)| \\
&\quad + (\Delta t)^2\, O\left(\frac{\Delta t}{K_d S}\right)
\end{aligned}$$

With a recurrence argument and thanks to equations (92) and (93) and same kind on formulas for Y_p and V_p, one prove that the scheme is convergent with a first order accuracy. In particular, it is has the great advantage to be unconditionally stable, which is bot the case of the classical explicit Euler discretisation.

References

[1] L. Martinez, A. Benkenida, B. Cuenot, A model for the injection boundary conditions in the context of 3D simulation of diesel spray: methodology and validation, Fuel 89(1) (2010) 219–228.

[2] D. Kah, Taking into account polydispersity in the framework of a coupled Euler-Lagrange approach for the modeling of liquid fuel injection in internal combustion engines, Ph.D. thesis, Ecole Centrale de Paris, 2010. Available online at http://tel.archives-ouvertes.fr/tel-00618786/en/.

[3] A. Vié, S. Jay, B. Cuenot, M. Massot, Accounting for polydispersion in the eulerian large eddy simulation of an aeronautical-type configuration, Submitted to Flow Turbulence and Combustion (2011).

[4] F. Doisneau, F. Laurent, A. Murrone, J. Dupays, M. Massot, Eulerian multi-fluid models for the simulation of dynamics and coalescence of particles in solid propellant combustion, Submitted to J. Comput. Phys. (2011). Available online at http://hal.archives-ouvertes.fr/hal-00618806/en.

[5] F. A. Williams, Spray combustion and atomization, Phys. Fluids 1 (1958) 541–545.

[6] F. A. Williams, Combustion Theory (Combustion Science and Engineering Series), ed F A Williams (Reading, MA: Addison-Wesley), 1985.

[7] G. A. Bird, Molecular gas dynamics and the direct simulation of gas flows, Oxford Science Publications 42 (1994).

[8] M. Garcia, Development and validation of the Euler-Lagrange formulation on a parallel and unstructured solver for large-eddy simulation, Ph.D. thesis, Université Toulouse III, 2009.

[9] A. Tagliani, Hausdorff moment problem and maximum entropy: a unified approach, Appl. Math. Comput. 105 (1999) 291–305.

[10] J. Greenberg, I. Silverman, Y. Tambour, On the origin of spray sectional conservation equations, Combustion and Flame 93 (1993) 90–96.

[11] F. Laurent, M. Massot, Multi-fluid modeling of laminar poly-dispersed spray flames: origin, assumptions and comparison of the sectional and sampling methods, Combust. Theory and Modelling 5 (2001) 537–572.

[12] R. McGraw, Description of aerosol dynamics by the quadrature method of moments, Aerosol Science and Technology 27 (1997) 255–265.

[13] D. L. Marchisio, R. O. Fox, Solution of population balance equations using the direct quadrature method of moments, Journal of Aerosol Science 36 (2005) 43–73.

[14] J. Mossa, Extension polydisperse pour la description Euler-Euler des écoulements diphasiques réactifs, Ph.D. thesis, Institut National Polytechnique de Toulouse, 2005.

[15] M. Massot, F. Laurent, D. Kah, S. de Chaisemartin, A robust moment method for evaluation of the disappearance rate of evaporating sprays, SIAM J. Appl. Math. 70 (2010) 3203–3234.

[16] F. Laurent, Numerical analysis of eulerian multi-fluid models in the context of kinetic formulations for dilute evaporating sprays, Mathematical Modeling and Numerical Analysis 3 (2006) 431–468.

[17] R. O. Fox, F. Laurent, M. Massot, Numerical simulation of spray coalescence in an eulerian framework: direct quadrature method of moments and multi-fluid method, Journal of Computational Physics 227 (2008) 3058–3088.

[18] L. R. Mead, N. Papanicolaou, Maximum entropy in the problem of moments, J. Math. Phys. 25 (1984) 2404–2417.

[19] H. Dette, W. J. Studden, The theory of canonical moments with applications in statistics, probability, and analysis, Wiley Series in Probability and Statistics: Applied Probability and Statistics, John Wiley & Sons Inc., New York, 1997. A Wiley-Interscience Publication.

[20] D. Kah, F. Laurent, M. Massot, S. Jay, A high order moment method simulating evaporation and advection of a polydisperse spray, In Press, J. Comput. Phys. (2011). Doi:10.1016/j.jcp.2011.08.032.

[21] D. L. Wright, Numerical advection of moments of the particle size distribution in Eulerian models, Journal of Aerosol Science 38 (2007) 352–369.

[22] D. Kah, M. Massot, Q. Tran, S. Jay, F. Laurent, A high order moment method with mesh movement for the description of a polydisperse evaporating spray, in: Proceedings of the International Conference on Multiphase Flows, Tampa, Florida (2010), pp. 1–15. Available online at http://hal.archives-ouvertes.fr/hal-00498214/en/.

[23] J. Bohbot, N. Gillet, A. Benkenida, IFP-C3D: an unstructured parallel solver for reactive compressible gas flow with spray, Oil & Gas Science and Technology 64(3) (2009) 309–335.

[24] C. Yuan, R. Fox, Conditional quadrature method of moments for kinetic equations, Journal of Computational Physics 230(22) (2011) 8216–8246.

[25] A. Kociszewski, On the calculations of maximum entropy distributions having prescribed the moments, J. Phys.A:Math. Gen. 18 (1985) L337–L339.

[26] D. Wright, Numerical advection of moments of the particule size distribution in eulerian models, Journal of Aerosol Science 38(3) (2007) 352–369.

[27] J. Reveillon, C. Péra, M. Massot, R. Knikker, Eulerian analysis of the dispersion of evaporating polydispersed sprays in a statistically stationary turbulent flow, Journal of Turbulence 5 (2004) 1–27.

[28] M. Massot, Eulerian multi-fluid models for polydisperse evaporating sprays, volume 492 of *CISM Courses and Lectures*, Springer Wien New York (2007), pp. 79–123. D.L. Marchisio and R.O. Fox Editors.

[29] M. Massot, F. Laurent, S. de Chaisemartin, L. Fréret, D. Kah, Eulerian multi-fluid models: modeling and numerical methods, in: Modelling and Computation of Nanoparticles in Fluid Flows, Lectures Notes of the von Karman Institute, NATO RTO-EN-AVT-169, 2009, pp. 1–86. Available online at http://www.rta.nato.int/Pubs/RDP.asp?RDP=RTO-EN-AVT-169.

[30] H. Meftah, Simulation Numérique Directe d'un spray en évaporation : Analyse et modélisation du mélange turbulent et des transferts thermiques, Ph.D. thesis, INSA de Rouen, France, 2008.

[31] J. Reveillon, DNS of Spray Combustion, Dispersion Evaporation and Combustion, volume 492 of *CISM Courses and Lectures*, Springer Wien New York (2007), p. 229. D.L. Marchisio and R.O. Fox Editors.

[32] J. Reveillon, F. Demoulin, Effects of the preferential segregation of droplets on evaporation and turbulent mixing, Journal of Fluid Mechanics 583 (2007) 273–302.

[33] M. Klein, A. Sadiki, J. Janicka, A digital filter based generation of inflow data for spatially developing direct numerical or large eddy simulations, J. Comput. Phys. 186 (2003) 652–665.